Universidad de Investigación de Tecnología Experimental YACHAY

Escuela de Ciencias Físicas y Nanotecnología

TÍTULO: Computational studies on the atomic and electronic structure of $\gamma - Al_2O_3$ surfaces

Trabajo de integración curricular presentado como requisito para la obtención del título de Físico

Autor:

Ayala León María Paula

Tutor:

PhD. Pinto Esparza Henry

Urcuquí, Julio 2022

Urcuquí, 21 de julio de 2022

SECRETARÍA GENERAL
(Vicerrectorado Académico/Cancillería)

CARRERA DE null
ACTA DE DEFENSA No. UITEY-PHY-2022-00012-AD

En la ciudad de San Miguel de Urcuquí, Provincia de Imbabura, a los 21 días del mes de julio de 2022, a las 09:00 horas, en el Aula S_CAN de la Universidad de Investigación de Tecnología Experimental Yachay y ante el Tribunal Calificador, integrado por los docentes:

Presidente Tribunal de Defensa	Dr. CHIMBORAZO GUERRON, JOHNNY FABRICIO , Ph.D.
Miembro No Tutor	LAGOS LLAGUNO, DANIEL ALEJANDRO , Ph.D.
Tutor	Dr. PINTO ESPARZA, HENRY PAUL , Ph.D.

El citado trabajo de titulación, fue debidamente aprobado por el(los) docente(s):

Tutor	Dr. PINTO ESPARZA, HENRY PAUL , Ph.D.

Y recibió las observaciones de los otros miembros del Tribunal Calificador, las mismas que han sido incorporadas por el(la) estudiante.

Previamente cumplidos los requisitos legales y reglamentarios, el trabajo de titulación fue sustentado por el(la) estudiante y examinado por los miembros del Tribunal Calificador. Escuchada la sustentación del trabajo de titulación, que integró la exposición de el(la) estudiante sobre el contenido de la misma y las preguntas formuladas por los miembros del Tribunal, se califica la sustentación del trabajo de titulación con las siguientes calificaciones:

Tipo	Docente	Calificación
Miembro Tribunal De Defensa	LAGOS LLAGUNO, DANIEL ALEJANDRO , Ph.D.	9,8
Tutor	Dr. PINTO ESPARZA, HENRY PAUL , Ph.D.	10,0
Presidente Tribunal De Defensa	Dr. CHIMBORAZO GUERRON, JOHNNY FABRICIO , Ph.D.	8,8

Lo que da un promedio de: **9.5 (Nueve punto Cinco)**, sobre 10 (diez), equivalente a: **APROBADO**

Para constancia de lo actuado, firman los miembros del Tribunal Calificador, el/la estudiante y el/la secretario ad-hoc.

Johnny Chimborazo

Dr. CHIMBORAZO GUERRON, JOHNNY FABRICIO , Ph.D.
Presidente Tribunal de Defensa

Henrypinto.

Dr. PINTO ESPARZA, HENRY PAUL , Ph.D.
Tutor

Daniel

LAGOS LLAGUNO, DANIEL ALEJANDRO , Ph.D.
Miembro No Tutor

DE LA CRUZ ZAPATA, TANIA DANIELA
Secretario Ad-hoc

AUTORÍA

Yo, **MARÍA PAULA AYALA LEÓN**, con cédula de identidad 0705008654, declaro que las ideas, juicios, valoraciones, interpretaciones, consultas bibliográficas, definiciones y conceptualizaciones expuestas en el presente trabajo; así cómo, los procedimientos y herramientas utilizadas en la investigación, son de absoluta responsabilidad de la autora del trabajo de integración curricular. Así mismo, me acojo a los reglamentos internos de la Universidad de Investigación de Tecnología Experimental Yachay.

Urcuquí, Julio 2022.

MARIA PAULA
AYALA LEON
Digitally signed by MARIA
PAULA AYALA LEON
Date: 2022.07.22 11:27:06
-05'00'

María Paula Ayala León
CI: 0705008654

AUTORIZACIÓN DE PUBLICACIÓN

Yo, **MARÍA PAULA AYALA LEÓN,** con cédula de identidad 0705008654, cedo a la Universidad de Investigación de Tecnología Experimental Yachay, los derechos de publicación de la presente obra, sin que deba haber un reconocimiento económico por este concepto. Declaro además que el texto del presente trabajo de titulación no podrá ser cedido a ninguna empresa editorial para su publicación u otros fines, sin contar previamente con la autorización escrita de la Universidad.

Asimismo, autorizo a la Universidad que realice la digitalización y publicación de este trabajo de integración curricular en el repositorio virtual, de conformidad a lo dispuesto en el Art. 144 de la Ley Orgánica de Educación Superior

Urcuquí, Julio 2022.

MARIA PAULA
AYALA LEON

Digitally signed by
MARIA PAULA AYALA
LEON
Date: 2022.07.22
11:27:33 -05'00'

María Paula Ayala León
CI: 0705008654

Acknowledgements

Primeramente, mis agradecimientos van para Dios y mi familia, porque siempre me han apoyado y guíado en la búsqueda de una carrera que me apasione y motive. Esto no hubiera sido posible sin el amor y alegría que me han brindado todos estos años.

Este trabajo se realizó bajo la guía del profesor Henry Pinto, a quien quisiera agradecer por ser un gran mentor y ayudarme en mi formación científica. Agradezco la oportunidad de formar parte de su grupo de investigación y aprender junto con mis compañeros. Sin duda ha sido una experiencia muy enriquecedora.

Igualmente, quisiera agradecer en general a todos quienes han hecho mi experiencia en Yachay Tech realmente increíble. Por supuesto, esto incluye a mis profesores desde Tronco Común hasta Carrera, quienes me transmitieron su amor por la ciencia con gran dedicación y paciencia. También un agradecimiento especial a los chicos de la AEFN-YT y Optica Student Chapter con quienes hemos vivido grandes aventuras. Asimismo, a mis queridas amigas de ConCiencia WY con quienes hemos formado un gran lazo, les deseo todo el éxito!

Finalmente, agradezco de corazón, por los amigos verdaderos que me dio la Universidad. A Cristina, por brindarme la mejor amistad de todas, por las aventuras vividas, por todo el cariño y momentos de calidad. A Mateo, por mostrarme siempre su apoyo, por las risas y momentos que contribuyeron a que esta experiencia sea muy especial. A Tony y a Carlitos, por todos los momentos juntos durante la carrera y esa gran amistad que estoy segura de que será duradera. A mis antiguas compañeras de cuarto, a mis compañeros de clase y todos los estudiantes de Yachay que son personas inspiradoras.

¡Gracias infinitas por brindarme la mejor experiencia de mi vida!

Resumen

$\gamma - Al_2O_3$ es un material importante para muchas aplicaciones industriales, tales como en petroquímica, industria automotriz, y especialmente en catálisis, debido a su gran área superficial. A pesar de que este material tiene gran relevancia tecnológica, su estructura atómica es desconocida. Puesto que, tener la estructura atómica adecuada es crucial para entender y mejorar las propiedades de este material, éste es un campo de investigación activo con muchas preguntas abiertas. Por lo tanto, en este trabajo realizamos estudios de DFT en las superficies de $\gamma - Al_2O_3$ usando dos de los modelos teóricos propuestos más citados en la literatura: Pinto (Modelo 1) y Digne (Modelo 2). Se realizó el análisis de las configuraciones electrónicas de la estructura del bulk, y de las superficies (111), (001), (110) para ambos modelos. Adicionalmente, las energías superficiales se calcularon para determinar que las superficies (111)a and (111), fueron las más energéticamente favorables para el Modelo 1 y 2, respectivamente. Partiendo de las superficies más estables en cada Modelo, se obtuvieron superficies no estequiométricas generando vacancias de oxígeno. Finalmente, los espectros UPS y las funciones de trabajo fueron simuladas para los casos más estables. Estos resultados pueden ser contrastados con experimentos futuros para corroborar los exactitud de los modelos.

Palabras clave: $\gamma - Al_2O_3$, SCAN, VASP, DFT, superficies, UPS, funciones de trabajo, energía superficial.

Abstract

$\gamma - Al_2O_3$ is an important material for many industrial applications, such as petrochemistry, automotive and especially in catalysis, due to its large surface area. Even though, this material has great technological relevance, its atomic structure it is still unknown. Given that, having the proper atomic structure of this material is crucial to understanding and improving its properties, this is an active field of research with many open questions. So, in this work we perform DFT studies in $\gamma - Al_2O_3$ surfaces using two of the most cited theoretical models proposed in the literature: Pinto (Model 1) and Digne (Model 2). The analysis of the electronic configurations of the bulk structure and the surfaces $(111), (001)$ and (110) was done for both models. Additionally, the surface energies were computed to determine that the surfaces $(111)a$, and (111) were the most energetically favorable for Model 1 and 2, respectively. From the most stable surfaces in each Model, non-stoichiometric surfaces were obtained by generating O vacancies. Finally, UPS spectra and work functions were simulated for the most stable cases. These results can be used to contrast with future experiments and test the accuracy of the Models.

Keywords: $\gamma - Al_2O_3$, SCAN, VASP, DFT, surfaces, UPS, work function, surface energy.

Contents

Acknowledgements **v**

Resumen **vii**

Abstract **ix**

List of Figures **xiii**

List of Tables **xvii**

1 Introduction **1**
- 1.1 Problem Statement . . . 2
- 1.2 General and Specific Objectives . . . 2

2 Theoretical Background **5**
- 2.1 Density Functional Theory . . . 5
  - 2.1.1 Many-Body Schrödinger Equation . . . 5
  - 2.1.2 Hartree-Fock equations . . . 7
  - 2.1.3 DFT principles . . . 9
  - 2.1.4 Functionals . . . 11
  - 2.1.5 Pseudopotentials . . . 12
- 2.2 Ultraviolet Photoelectron Spectroscopy (UPS) . . . 13
- 2.3 Surface Energy . . . 14
  - 2.3.1 Stoichiometric surfaces . . . 15
  - 2.3.2 Non-stoichiometric surfaces . . . 16

3 Computational Method **17**
- 3.1 VASP . . . 17
- 3.2 Bulk system . . . 17
- 3.3 Surfaces . . . 18

4 Results & Discussion **21**
4.1 Bulk structure 21
4.1.1 Model 1 (M1) 21
4.1.2 Model 2 (M2) 24
4.2 Surfaces 25
4.2.1 Stoichiometric surfaces 25
4.2.2 Most stable surfaces 31
4.2.3 Non-stoichiometric surfaces 33

5 Conclusions & Outlook **41**

A Appendix A **43**

B Appendix B **47**

C Appendix C **49**

Bibliography **51**

List of Figures

2.1 Jacob's ladder of density functional theory[1], where the different families of functionals are listed in a scheme from the least (bottom) to the most (top) accurate tools 11

2.2 Adapted from ref.[2]. Representation of a pseudopotential. The solid lines represent the exact wave function Ψ and potential, while the dashed lines are the approximations with a pseudopotential . . . 13

2.3 Graphical description of Eq.2.26 that describes the mechanism of the PAW pseudopotential. Taken from ref.[3] 14

2.4 Adapted from ref.[4]. The figure shows the IMFP of a sample where the y axis is in Å. The yellow region correspond to energies around $40 - 70 eV$, that are related to IMFP of around $3 - 7$Å. This means that for this energy range, the photons will penetrate that distance into the surface 15

3.1 **(a)** Perfect cubic spinel system showing the (111) surface plane. **(b)** Defective spinel system (M1) showing the (010) surface plane which shows equivalent atomic organization as in (a). **(c)** Non-defective spinel system (M2) showing the (032) surface plane which shows equivalent atomic organization as in (a) 19

3.2 General view of the NIST Electron Inelastic-Mean-Free-Path Database[5]. Starting from the upper left side, the images show the steps to get the IMFP from inorganic compounds using the predictive formula (Eq. 3.3) 20

4.1 Results of the static calculations in M1 for the **(a)** Total Energy vs. ENCUT energy and **(b)** Total Energy vs. KPOINTS computations 21

4.2 Data for the Total Energy calculations with respect to the cell volume (red dots) and the fitting with the Birch-Murnaghan Equation of State (blue solid line) for M1. 22

4.3 Defective spinel bulk system for Model 1 (M1). The tetrahedal Al_A, and octahedral Al_B atoms are represented in purple and blue, respectively. The vacancies are represented with black and grey spheres and the O atoms are the red spheres. 22

4.4 SCAN computed DOS for system M1. The line represents the Fermi level at zero and it is observed a bandgap of $E_g^{M1} = 4.9$ eV 24

4.5 Results of the static calculations in M2 for the **(a)** Total Energy vs. ENCUT energy and **(b)** Total Energy vs. KPOINTS computations 24
4.6 Data for the Total Energy calculations with respect to the cell volume (red dots) and the fitting with the Birch-Murnaghan Equation of State (blue solid line) for M2. 25
4.7 Non-defective spinel bulk system for Model 2 (M2). The tetrahedal Al_A, and octahedral Al_B atoms are represented in purple and blue, respectively. The O atoms are the red spheres. 25
4.8 SCAN computed DOS for system M1. The line represents the Fermi level at zero and it is observed a bandgap of E_g^{M1} = 4.9 eV 27
4.9 **(a)** Side and **(b)** top view of surface (111)a for M1. The circles in part (b) correspond with the atoms with arrows in part (a) 28
4.10 **(a)** Side and **(b)** top view of surface (111)b for M1. The circles in part (b) correspond with the atoms with arrows in part (a) 28
4.11 Surface (111)b plane for M2 29
4.12 Side view of the surfaces **(a)** (001)a and **(b)** (001)b for M1. 29
4.13 Side view of the surfaces **(a)** (001)a and **(b)** (001)b for M2. 30
4.14 Side view of the surfaces **(a)** (110)a, **(b)** (110)b and **(c)** (110)c for M1. 30
4.15 Side view of the surfaces **(a)** (110)a and **(b)** (110)b for M2. 31
4.16 PDOS of the surfaces **(a)** $(111)a$ and **(b)** $(001)a$ of system M1. The Fermi level is represented by the line 33
4.17 PDOS of the surfaces **(a)** (111) and **(b)** $(001)a$ of system M2. The Fermi level is represented by the line 34
4.18 UPS of the surfaces **(a)** $(111)a$ with a workfunction of $\phi = -4.7eV$ and **(b)** $(001)a$ with a workfunction of $\phi = 7.7eV$ of M1 considering the atomic orbital contribution 34
4.19 UPS of the surfaces **(a)** (111) with a workfunction of $\phi = 6.3eV$ and **(b)** $(001)a$ with a workfunction of $\phi = 6.2eV$ of M2 considering the atomic orbital contribution 35
4.20 Comparison of the total UPS spectra of the most stable surfaces for Model 1 and 2 with the experimental UPS of $\gamma - Al_2O_3$ thin films obtained in ref.[6] 35
4.21 Top view of the non-stoichiometric surfaces type a in a **(a)** trigonal and **(b)** rectangular configuration. The green and yellow spheres are the vacancies type a 36
4.22 Non-stoichiometric surfaces type b in a **(a)** trigonal and **(b)** rectangular configuration. The yellow spheres represent the vacancies type b 36
4.23 Non-stoichiometric surface type ab in the trigonal configuration. The colored spheres represent the vacancies 37
4.24 Non-stoichiometric surfaces with two vacancies of the same type, where **(a)** is the aa case, **(b)** is the aa2 case and **(c)** is the bb case. The colored spheres represent the vacancies 37
4.25 Non-stoichiometric surfaces with two vacancies of the different type, where **(a)** is the ab1 case, **(b)** is the ab2 case and **(c)** is the ab3 case. The colored spheres represent the vacancies 38
4.26 Surface energy of the non-stoichiometric surfaces of Model 1 38

4.27 Non-stoichiometric surfaces of Model 2. **(a)** Type ov1 and **(b)** Type ov2. The colored spheres represent the vacancies 39
4.28 Surface energy of the non-stoichiometric surfaces of Model 2. 40

A.1 Detailed computed PDOS for the surface (111)*a* studied in M1 43
A.2 Detailed computed PDOS for the surface (001)*a* studied in M1 44
A.3 Detailed computed PDOS for the surface (111) studied in M2 44
A.4 Detailed computed PDOS for the surface (001)*a* studied in M2 45
A.5 PDOS of the rest of the surfaces generated for M1 45
A.6 PDOS of the rest of the surfaces generated for M2 45

B.1 Photoionization Cross Section used to simulate the UPS. Taken from ref.[7] 47
B.2 IMFP used to simulate the UPS 48

C.1 Computed workfunction for the surface (111)*a* of M1 49
C.2 Computed workfunction for the surface (001)*a* of M1 50
C.3 Computed workfunction for the surface (111) of M2 50
C.4 Computed workfunction for the surface (001)*a* of M2 50

List of Tables

4.1 Crystallographic data of $\gamma - Al_2O_3$ for Model 1. 23
4.2 Crystallographic data of $\gamma - Al_2O_3$ for Model 2. 26
4.3 Surface energy σ calculations of the relaxed slabs in different surfaces for the cubic system of $\gamma - Al_2O_3$ in the model 1 32
4.4 Surface energy σ calculations of the relaxed slabs in different surfaces for the cubic system of $\gamma - Al_2O_3$ in the model 2 32

Chapter 1

Introduction

Nanomaterials have supposed an important breakthrough for the improvement of many applications. Catalysis is one of the fields that has benefited a lot from nanostructures, which can be used as catalysts or as a support for catalysis. This field in general is of great importance for the industry, since 75% of all the chemicals are produced by this mean[8], as well as in the global economy, where catalysis process are associated with approximately 30% of European gross domestic product[9].

Currently, a very important material for catalysis applications is $\gamma - Al_2O_3$, which is a metastable phase of Al_2O_3. Its synthesis is commonly done via thermal dehydration of boehmite that undergoes phase transitions when temperature increases. The transitions generally occur in this order: boehmite $\rightarrow \gamma \rightarrow \delta \rightarrow \theta \rightarrow \alpha$, being $\alpha - Al_2O_3$ the most stable[10]. However, it was reported[11] that $\gamma - Al_2O_3$ is more thermodynamically stable than the α phase at specific surface areas greater than $75m^2g^{-1}$. It is precisely, due to this large surface area, among its pore volume and size distribution, why $\gamma - Al_2O_3$ is suitable for catalysis applications[12].

The usefulness of $\gamma - Al_2O_3$ for applications in catalysis is very wide. For instance, it acts as a support for Co-based catalysts in the production of clean fuels[13]. Likewise, it has been used as a catalyst support for CoMoS or NiMoS phases in the refining industry[14]. However, in this process there are still some challenges to address like the dissolution or dehydration of this material during catalytic processes[13]. Additionally, this material can be used for other applications like petrochemistry[15], automotive industry[16] and the dehydration of alcohols[17]. Furthermore, a recent experimental work demonstrated that $\gamma - Al_2O_3$ works well as an activated surface for the removing of fluoride from water.[18]

It is clear that $\gamma - Al_2O_3$ has a great relevance in many fields, but as was said before, there are still some problems related to its usage. An accurate way to find solutions for these problems is, for instance, to understand how the catalytic reactions occur, which can be done via simulations. However, theoretical studies in this material are a challenging task because they require performing surface analysis, but for that, it is necessary to start from the bulk structure of the material[19]. This is a major issue, since the atomic structure of $\gamma - Al_2O_3$ remains unknown[16].

In the literature, there has been a tremendous effort for revealing the actual crystal structure of this material, since the earliest works on this matter that date back to 1935[20]. Those works have been summarized in these reviews[21,19,16,17,22]. Among the most cited atomic models are the cubic models of Smrcok[23] and Digne[15], and the non-cubic models from Pinto[24] and Paglia[25]. These models have been proposed considering the different information that has been possible to obtain with experimental data. The experimental techniques used so far to characterize this material are Infrared (IR), X-ray diffraction (XRD), nuclear magnetic resonance (NMR), Transmission electron microscopy (TEM), selected area electron diffraction (SAED)[16] and Ultraviolet Photoelectron Spectroscopy (UPS)[6].

1.1 Problem Statement

The unstable nature of $\gamma - Al_2O_3$ makes it really hard to perform experimental characterization of this material. This constitutes a problem in the search for the actual atomic structure, since the theoretical models are usually validated with experimental results.

First of all, it is a hard task to synthesize a highly, pure crystalline $\gamma - Al_2O_3$ due to the conditions needed to get the phase transition. Thus, without proper samples, the experimental data can lead to wrong conclusions. Additionally, the most common characterization technique used is XRD, which in principle has been useful to determine lattice parameters, but the spectra for $\gamma - Al_2O_3$ samples look really similar to other phases. This generates a high difficulty when it comes to choose suitable results for comparison with theoretical models[16,19,26]. On the other hand, UPS is a surface sensitive technique, ideal for catalytic active materials, which can be a good approach to obtain reliable information on this material. However, I have only found one experimental work on UPS characterization of this material[6].

Alongside the experimental challenges, the theoretical work in this area also has several complications. At the moment of deciding how should be the atomic structure of $\gamma - Al_2O_3$, there are several questions that has not been answered for more than twenty years. These questions are: is this material completely dehydrated? does it contain Al vacancies? is it in general a cubic structure? is it a spinel-like structure? After many years of research, some authors report that spinel-like structures with vacancies are in more agreement with experiments, but there are still a lot of points that need to be understood first before finding the actual structure. DFT has been the most used tool for the theoretical description of this material[16].

In this work, I am going to test two of the most cited $\gamma - Al_2O_3$ models (Pinto and Digne), by performing different simulations with a more sophisticated DFT functional (SCAN) compared to the functional used in those works (GGA). I will also focus on acquiring UPS simulations of the surfaces to have available theoretical data on this particular technique. Finally, I am going to study non-stoichiometric systems, to understand the behaviour in the presence of different atmospheres.

1.2 General and Specific Objectives

The general objective of this work is to perform DFT calculations on $\gamma - Al_2O_3$ surfaces by using a state-of-the-art functional and two atomic models (Model 1 and Model 2) of the material available in the literature. To accomplish this, the following specific objectives are needed:

- Explain the theoretical formalism behind DFT, including the basic aspects of the state-of-the-art SCAN functional
- Study the electronic structure and the optimized bulk structure systems of Models 1 and 2.
- Construct stoichiometric surfaces for each Model using the bulk structures as starting points.
- Calculate the surface energy of all the surfaces for Models 1 and 2, to determine the most stable configuration in each case.
- Generate non-stoichiometric surfaces from the most stable surfaces in each Model
- Galculate the surface energy for all the non-stoichiometric surfaces to determine the most stable ones in each Model.
- Perform UPS simulations as well as the calculation of the work functions for stoichiometric surfaces in Models 1 and 2.
- State the conclusions of the work by comparing the results with the available experiments.

Chapter 2

Theoretical Background

This section, is devoted to show the process of linking first principle approaches to the description of a real material. The important concepts and mathematical formalism related to the modelling of a many-electron system are going to be described. Likewise, the theory related to the description of material's properties is going to be explained by introducing the Surface Energy concepts and the Ultraviolet Photoelectron Spectroscopy Simulation (UPS) framework.

2.1 Density Functional Theory

2.1.1 Many-Body Schrödinger Equation

Nowadays, it has been shown in many fields that significant enhancement of different properties can be achieved by understanding a system at a fundamental level. For applications in Condensed Matter Physics, this usually means the study of the atomic and electronic structure of a material. In this scenario, Quantum Mechanics plays a fundamental role in the description of matter, where the Schrödinger Equation will provide the relevant information about a quantum system. However, this equation can only be solved exactly for a system with one electron (Hydrogen atom)[27]. When, the system becomes larger and more complicated (more electrons and nuclei), it is described by a *many-body* wave function Ψ (Eq. 2.1) that will depend in the electron ($\vec{r_i}, i = 1, ..., N$) and nuclei ($\vec{R_i}, i = 1, ..., M$) coordinates. Also, for many applications, it is important to define the **Electron Density** $n(r)$ (Eq. 2.2) which is *"the probability of finding any electron at position* ***r****"*[28]. Therefore, the integration of $n(r)$, along the whole material is equal to the total number of electrons N, since Ψ is normalized to unity[28].

$$\Psi = \Psi(r_1, r_2, ..., r_N; R_1, R_2, ..., R_M) \tag{2.1}$$

$$n(r) = N \int |\Psi(r, r_2, ..., r_N; R_1, R_2, ..., R_M)|^2 dr_2 ... dr_N dR_1 ... dR_M \tag{2.2}$$

On the other hand, Ψ satisfies the time-independent Many-body Schrodinger equation (Eq. 2.3), where the lowercase and uppercase indexes are related to the electron and nuclei coordinates, respectively. The factors Z_I and Z_J are the atomic numbers of atoms I and J. The terms inside the brackets constitute the Hamiltonian H of the system and have all the interactions that the electron and nuclei can perceive. The first two terms in H are the kinetic energies of the electron and nuclei ($\hat{T}$), while the third and fourth terms correspond to the repulsive Coulomb's interaction between electron-electron (V_{e-e}) and nucleus-nucleus (V_{n-n}). The last term in H is the attractive Coulomb's interaction between the electrons and the nuclei (V_{e-n}). Although, this equation contains all the information to describe the properties of any system, it is practically impossible to solve due to its high complexity[28]. An important point is that, Eq. 2.3 only requires fundamental constants that are independent of any material and no empirical information is needed (first principle approach).

$$\left[-\sum_{i}\frac{\hbar^2}{2m_e}\nabla_i^2-\sum_{I}\frac{\hbar^2}{2m_I}\nabla_I^2+\frac{1}{2}\sum_{i\neq j}\frac{e^2}{4\pi\epsilon_o}\frac{1}{|r_i-r_j|}+\frac{1}{2}\sum_{I\neq J}\frac{e^2}{4\pi\epsilon_o}\frac{Z_IZ_J}{|R_I-R_J|}-\sum_{i,I}\frac{e^2}{4\pi\epsilon_o}\frac{Z_I}{|r_i-R_I|}\right]\Psi=E_{TOT}\Psi \tag{2.3}$$

It is possible to simplify Eq. 2.3 by re-arranging the units considering the relevant energy scales. The average orbital radius of the H atom at the fundamental state is $a_o \approx 0.529$Å. Also, from Coulomb's interaction in the system, one can get the energy associated that is called Hartree energy (Eq. 2.4). Then, using a semi-classical argument, setting $e = 1$ and the Bohr model for the H atom it is possible to re-write Eq. 2.3 in "Hartree-atomic units" (Eq. 2.5)[28]. The relation with the S.I. system is given by:

$$\begin{aligned}1\text{Ha} &= 27.2114eV = 4.3596 * 10^{-18}J\\ 1\text{bohr} &= 0.529177\text{Å} = 0.529177 * 10^{-10}m\\ 1\text{a.u. of mass} &= 9.10938291 * 10^{-31}kg\end{aligned}$$

$$E_{Ha}=\frac{e^2}{4\pi\epsilon_o a_o} \tag{2.4}$$

$$\left[-\sum_{i}\frac{\nabla_i^2}{2}-\sum_{I}\frac{\nabla_I^2}{2m_I}+\frac{1}{2}\sum_{i\neq j}\frac{1}{|r_i-r_j|}+\frac{1}{2}\sum_{I\neq J}\frac{Z_IZ_J}{|R_I-R_J|}-\sum_{i,I}\frac{Z_I}{|r_i-R_I|}\right]\Psi=E_{TOT}\Psi \tag{2.5}$$

Now, Eq. 2.5 becomes easier to handle, since the number of constants have been reduced. Nevertheless, it still depends in too many variables. Another simplification to this equation is to apply the Born-Oppenheimer Approximation[29], which states that the electronic and nuclei contribution to the overall wave function can be treated separately. Considering that the nuclei masses are around 10^5 times greater than the electron masses, it is possible to set the limit of $M_I \rightarrow \infty$, that causes the kinetic energy of the nuclei to become negligible. Using the same argument, it is fair to say that the nuclei are practically immobile as compared to the electrons, therefore the term V_{n-n} becomes a constant. If R_I is considered as an external parameter, such that the wave function Ψ only depends on the electron coordinates, the many-body Schrodinger equation has now the form of Eq. 2.6. which is known as the fundamental equation of electronic structure theory, following the treatment done by ref.[28].

$$\left[-\sum_i \frac{\nabla^2}{2} + \sum_i V_n(r_i) + \frac{1}{2}\sum_{i\neq j}\frac{1}{|r_i - r_j|}\right]\Psi = E\Psi \tag{2.6}$$

$$\text{with} \quad E = E_{TOT} - \frac{1}{2}\sum_{I\neq J}\frac{Z_I Z_J}{|R_I - R_J|} \quad \text{and} \quad V_n(r) = -\sum_I \frac{Z_I}{|r - R_I|}$$

2.1.2 Hartree-Fock equations

With the previous simplifications, it is possible to write the Many-electron Hamiltonian as Eq. 2.7, where Eq. 2.8 gives the single-electron Hamiltonian. Now, with the general idea of the terms involving the Hamiltonian, it is also important to think about other two aspects: (*i*) the shape of the wave function and (*ii*) how to include the repulsion between electrons in a simpler way.

$$\hat{H}(r_1, ..., r_N) = \sum_i \hat{H}_o(r_i) + \frac{1}{2}\sum_{i\neq j}\frac{1}{|r_i - r_j|} \tag{2.7}$$

$$\hat{H}_o(r) = -\frac{1}{2}\nabla^2 + V_n(r) \tag{2.8}$$

For point (*i*), it has to be considered that Ψ should obey Pauli's principle. The use of the Slater Determinant[27] formalism for a system with N electrons (Eq. 2.9) yields the right mathematical behaviour for Ψ, where the pre-factor is used for normalization purposes. The wave function in Eq. 2.9, depends on ϕ_i, which is a function that considers the electrons as if they were independent of each other. Here, N refers to the number of electrons and σ is a term that includes the information of the spin[27]. It is possible to prove[28] that the electron density in this scenario is actually the sum of the probabilities of the independent electrons (Eq.2.10).

$$\Psi_{HF}(r_1\sigma_1...r_N\sigma_N) = \frac{1}{\sqrt{N!}}\begin{vmatrix} \phi_1(r_1\sigma_1) & \phi_1(r_2\sigma_2) & ... & \phi_1(r_N\sigma_N) \\ \phi_2(r_1\sigma_1) & \phi_2(r_2\sigma_2) & ... & \phi_2(r_N\sigma_N) \\ . & . & . & . \\ . & . & . & . \\ . & . & . & . \\ \phi_N(r_1\sigma_1) & \phi_N(r_2\sigma_2) & ... & \phi_N(r_N\sigma_N) \end{vmatrix} \tag{2.9}$$

$$n(r) = \sum_i |\phi_i(r)|^2 \tag{2.10}$$

For the point (*ii*), it is used a classical concept related to the fact that, for a given distribution of electronic charge $n(r)$, an electrostatic potential φ that obeys Poisson's equation ($\nabla^2\varphi(r) = 4\pi n(r)$) is generated. Then, the electrons will be immersed in a electrostatic potential that is called Hartree Potential $V_H(r) = -\varphi(r)$. This potential can be included in Eq.2.7 as the term that accounts for the electron repulsion, resulting in the self-consistent set of equations

(Eqs. 2.11, 2.12, 2.13, that have to be solved simultaneously. For a given ϕ_i, $n(r)$ can be obtained and replaced in Eq. 2.13 to get V_H. Then, V_H is replaced in Eq. 2.11 to obtain ϕ_i again. The latter result is used in Eq. 2.12 to get $n(r)$ that should be equal or close enough to the initial density. The process is repeated until consistency is achieved. It is important to remark that the general form of V_H can be obtained from Eq.2.14.

$$\left[-\frac{\nabla^2}{2} + V_n(r) + V_H(r)\right]\phi_i(r) = \varepsilon_i\phi_i(r) \tag{2.11}$$

$$n(r) = \sum_i |\phi_i(r)|^2 \tag{2.12}$$

$$\nabla^2 V_H(r) = -4\pi n(r) \tag{2.13}$$

$$V_H(r) = \int dr' \frac{n(r')}{|r - r'|} \tag{2.14}$$

The set of self-consisted Equations 2.11-2.12, are the simplest approach to solve the many-body Schrodinger equation, but it considers electrons as classical particles. To take into account the quantum behaviour of these systems it is important to add a proper term that expresses the Coulombic repulsion. An accurate method for this task is to consider that this repulsion exists, but the interaction is not too strong. Therefore, it is possible to use Variational Principle[27], to account for this effect, but still recover solutions in the form of a Slater Determinant, that results in a electron density under the independent electron approximation. In this scenario, one can consider the ground state energy (2.15), and minimize this term with respect to ϕ_i functions (Eq. 2.16). After that, it is a matter of replacing Eq. 2.15 into Eq. 2.16 to obtain the **Hartree-Fock Equations** (Eq. 2.17), that now take in consideration the *Fock-exchange functional* (Eq. 2.18). The latter functional, is a sum over single occupied states that allows to account for quantum effects, but adds non-locality to the self-consistent equations, which means that now there are two variables involved (r, r')[28].

$$E = \left\langle \Psi \middle| \hat{H} \middle| \Psi \right\rangle \tag{2.15}$$

$$\frac{\delta E}{\delta \phi_i *} = 0 \tag{2.16}$$

$$\begin{gathered} \left[-\frac{\nabla^2}{2} + V_n(r) + V_H(r)\right]\phi_i(r) + \int dr' V_\chi(r, r')\psi(r') = \varepsilon_i\phi_i(r) \\ n(r) = \sum_i |\phi_i(r)|^2 \\ \nabla^2 V_H(r) = -4\pi n(r) \end{gathered} \tag{2.17}$$

$$V_\chi(r, r') = -\sum_j \frac{\phi_j^*(r')\psi_j(r)}{|r - r'|} \tag{2.18}$$

Nevertheless, the latter equations are not taking into account another relevant quantum effect. It is necessary to include a *correlation* term V_c, that results from the intuition that Coulomb repulsion will decrease the probability of finding an electron, due to the presence of another electron in close proximity[28]. Also, it is possible to simplify even more by considering a *local exchange potential* V_x. Then, Eq. 2.17 are modified by including the terms V_x and V_c.

2.1.3 DFT principles

Density Functional Theory (DFT) is a quantum mechanical method that solves approximate versions of the Schrodinger Equation. It is useful to calculate the electronic structure of atoms, molecules and solids[30], for different fields like catalysis, trace of impurities and even in planetary formation[31]. The main principle of this theory is the fact that, for calculating the ground state energy of a system, it is just necessary to focus on the electron density $n(r)$, rather than in the full wave function Ψ. This is a major benefit since it allows to go from a $3n$-dimensional equation (many-body Schrödinger equation) to n separate three dimensional equations, reducing the computational cost[32]. In this section, it is going to be described how the full wave function Ψ can be associated with the electron density by explaining the main theories that gave birth to this method.

Hohenberg-Khon theorem

The total energy of a system can be calculated using Eq. 2.15, where the Hamiltonian (Eq. 2.8) is general for any material. Thus, any change in E must be associated with changes in the wave function Ψ (E is a functional of Ψ). Using this idea, Hohenberg and Khon (1964) stated the main theorem in DFT: *"if E is the ground state energy, then E is a functional of the electron density only"* (Eq. 2.19).

$$E = F[n] \tag{2.19}$$

This theorem is based on three premises, whose proof is explained in ref.[28].

- For a given ground-state electron density $n(e)$, it is not possible to obtain two different external potentials V_n. Therefore, $V_n = F[n]$
- If the atomic configuration changes, it will change the wave function. Therefore, the external potential determines uniquely the wave function Ψ ($\Psi = F[Vn]$)
- As it was mentioned before, at any quantum state, the energy E is determined uniquely by the wave function $E = F[\Psi]$

Gathering these three points, one can observed a relation that goes like $n \rightarrow V_n \rightarrow \Psi \rightarrow E$. Consequently, it is obtained a final relation like Eq. 2.19, where it is concluded that only the electron density is necessary to calculate the ground-state energy.

Khon-Sham Equations

The Hohenberg-Khon theorem is a powerful tool, since it tells that to calculate the ground state energy is only needed the electron density instead of the full complex wave function. However, this theorem does not explain what is the form of the functional. Using the complete expression for E by replacing Eq. 2.8 into 2.15, and used the idea behind Eq. 2.19, one can get a general expression of the functional (Eq. 2.20)[28]. This equation is arranged in such way that all the unknown quantities are included in the last term that is called the *exchange and correlation energy*.

$$E = F[n] = \int drn(r)V_n(r) - \sum_i \int dr\phi_i^*(r)\frac{\nabla^2}{2}\phi_i(r) + \frac{1}{2}\iint drdr'\frac{n(r)n(r')}{|r-r'|} + E_{xc}[n] \tag{2.20}$$

Then, the ground state energy will be obtained by considering which functional $F[n]$ will minimize the total energy. Therefore, applying a similar approach as the one used in the Hartree-Fock equations, Eq. 2.21 yields to the *Khon-Sham equations* (Khon and Sham, 1965) (Eq. 2.22) Here, the terms of V_n and V_H were described previously, and V_{xc} is the *exchange and correlation potential* obtained with Eq. 2.23. The exact form of this potential remains unknown, but many approximations have been made with different levels of sophistication. Then, using also the expression for $n(r)$, this also become a self-consistent method.

$$\left.\frac{\delta F[n]}{\delta n}\right|_{no} = 0 \tag{2.21}$$

$$\left[-\frac{1}{2}\nabla^2 + V_n(r) + V_H(r) + V_{xc}(r)\right]\phi_i(r) = \varepsilon_i\phi_i(r) \tag{2.22}$$

$$V_{xc}(r) = \left.\frac{\delta E_{xc}[n]}{\delta n}\right|_{n(r)} \tag{2.23}$$

It is important to remark that here, ϕ_i are the single-electron wave functions. Depending in the system under study, a proper basis-set for the wave functions has to be chosen for Ψ_i. In the case of crystal modelling, it is used the Bloch's theorem[33] expressed as Eq. 2.24, where the first term is a plane wave times a function $\boldsymbol{u_{nk}}$ that contains the periodicity of the lattice. The subscripts n and k are used for the band index and **k** point in the Brillouin zone, respectively. Performing all the mathematical steps, it is arrived to Eq. 2.25, where Ω is the cell volume and the sum is over all the reciprocal lattice vectors $\boldsymbol{G} = m1\boldsymbol{b1} + m2\boldsymbol{b2} + m3\boldsymbol{b3}$ for integer values m_i. In principle, this Equation goes to infinity, but for computational modelling it is possible to truncate this sum up to some value that ensures an accurate result. This is going to be explained with more detail in the Chapter 3

$$\psi_{n\mathbf{k}}(r) = e^{i\boldsymbol{k}\cdot\boldsymbol{r}}u_{n\boldsymbol{k}}(r) \tag{2.24}$$

$$\psi_{n\boldsymbol{k}}(r) = \frac{1}{\sqrt{\Omega}}\sum_{\boldsymbol{G}} C_{n\boldsymbol{k}}e^{i(\boldsymbol{k}+\boldsymbol{G})\cdot r} \tag{2.25}$$

2.1.4 Functionals

Through the years, there have been many proposals[34] to approximate the functional term for V_{xc} with different levels of prediction and accuracy. Here, a brief description of some of the most used functionals it is going to be provided. In Fig. 2.1, it is shown the Jacob's ladder that is used to represent the different levels of sophistication regarding the functionals. The functionals in the ladder were constructed by considering different factors with a explicit form of the electron density. For the functionals with higher accuracy, it has also been considered some non-local effect by using a explicit dependence with orbitals. When climbing the ladder, the accuracy increases, but it comes with a significant cost in computational resources.

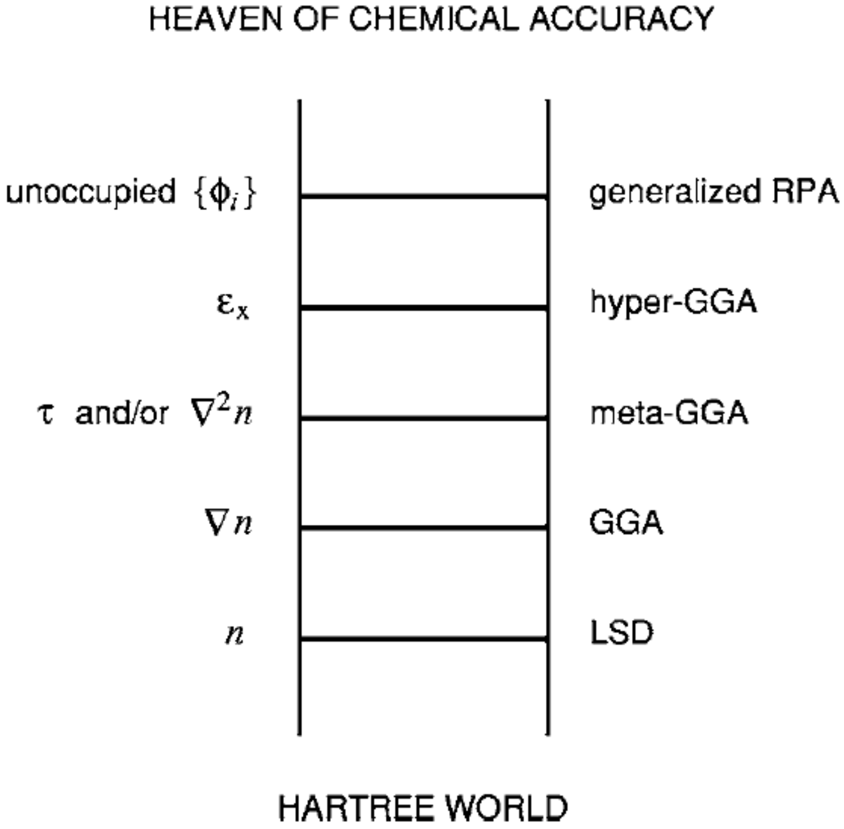

Figure 2.1: Jacob's ladder of density functional theory[1], where the different families of functionals are listed in a scheme from the least (bottom) to the most (top) accurate tools

The simplest proposal for a functional has been the **Local Density Approximation** (LDA)[35] or Local Spin Density Approximation (LSD), which is located at the bottom of the Jacob's latter. This model[28] uses the homogeneous electron gas problem, from which is possible to know the exact form of the exchange energy E_x and find a numerical solution for correlation energy E_c. Then, it is possible to approximate any material as it was composed by different regions with a differential volume where it is considered a local electron density $n(r)$. This is the simplest approximation, that can be used for some basic calculations, but it does not give good results for some molecular properties[36]. However, it has been the based for many other functional approaches. The next step is the **Generalized Gradient Approximation** (GGA)[1], that additionally contains the gradient of the electron density $\nabla n(r)$ and accounts for the effect that in reality, $n(r)$ is in fact, in-homogeneous, contrary to the assumptions made in LDA. This functional has achieved good accuracy for simulating chemical reactions and calculating surface energies, but it also overestimates lattice constants, band-gaps, Van der Waals forces and magnetization properties.[36],[37].

The next step is the **meta-GGA** approximation[1], which is considered a semi-local functional that takes into account the Laplacian of the density $\nabla^2 n(r)$ and the orbital's kinetic energy τ, that allows to satisfy more constraints. It has shown great improvements for many properties, specially in the prediction of type of bindings[36]. Under this approximation, it was proposed the **Strongly Constrained and Appropriately Normed semilocal density functional** (SCAN)[38]. This functional fulfills the 17 known constraints that arise from the semi-local terms and it is more predictive than the GGAs[36]. SCAN can predict geometries, energies, bonds, Van der Waals interactions, among other properties of molecules or crystals, improving the accuracy at lower costs[39].

2.1.5 Pseudopotentials

In Section 2.1.3, it was stated that at some point it is necessary to set a limit for the number of plane waves that are going to be used in the calculations. However, a basis that reproduces the exact behaviour of an atom, which has to take account the tightly bound nature of the electrons and the rapid oscillations of the wave functions (nodal features) near the core, will need a really high number of plane waves[2]. This upper limit will enhance the computational cost and timing. A good way to address this issue is to have in mind that it may not be necessary to include all the electrons of a material into the calculations, since most of the physical phenomena involve mainly the valence electrons. Therefore, one can use a Pseudopotential, which is a function that will simulate the effect of the core electrons for the valence electrons[31].

In Fig. 2.2, it is shown the general idea behind a pseudopotential. A modified potential $\tilde{V}$ is used to get a smooth pseudo-wave function $\tilde{\Psi}$, that will be easier to handle. Beyond a critical distance away from the nucleus (r_C), the approximations (dashed lines) and real quantities (solid lines), start to coincide in the region where the relevant chemistry occurs (green zone)[2]. Nevertheless, the pseudo-wave function used for the valence electrons should fulfill the orthogonality between the valence and core electron wave functions, meaning that it should contain nodes according to the expected core orbital behaviours[3],[2]. In this scenario, the first approaches to build a mathematical expression for a pseudopotential were the hard pseudopotential, norm-conserving pseudopotential, or ultrasoft pseudopotential pseudopotentials[40]. However, these pseudopotentials have some disadvantages since they either require a high number of plane waves, or they do not fulfill the orthogonality requirements[3].

In 1994, Blöchl proposed another formalisim for the pseudopotential called the Projector-Augmented-Wave method (PAW)[41], that solves the drawbacks from the other types of pseudopotentials. The idea is summarize in Eq. 2.26[3], where φ_v is the function that will be used to simulate the system as exact as possible. The first term $\tilde{\varphi_v}$ is a function that is exact outside the core region, while becomes smooth and inexact inside the core region. The second term χ_v is the opposite, since it is exact inside the core region and incorporates the node structures needed to accurately simulate the wave function in this zone, while outside it smoothly tends to zero. Finally, the last term $\tilde{\chi}_v$ helps to get the right behaviour in each zone, by being equal to $\tilde{\varphi}_v$ inside the core, so it can cancel out, and vice versa with the term $\tilde{\chi}_v$ (Fig. 2.3).

$$\varphi_v = \tilde{\varphi}_v + \chi_v - \tilde{\chi}_v \tag{2.26}$$

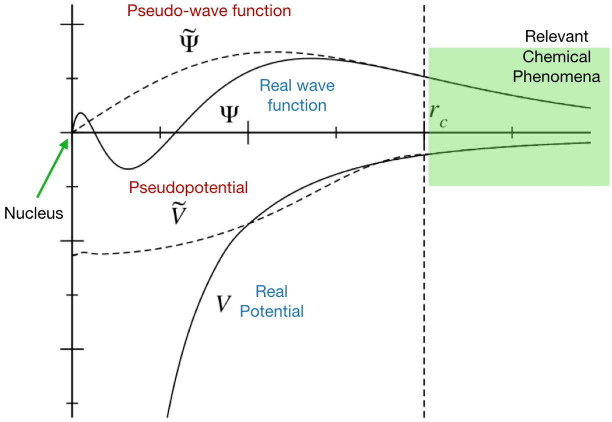

Figure 2.2: Adapted from ref.[2]. Representation of a pseudopotential. The solid lines represent the exact wave function Ψ and potential, while the dashed lines are the approximations with a pseudopotential

2.2 Ultraviolet Photoelectron Spectroscopy (UPS)

UPS is a characterization technique to determine the different types of bonding present in a material, that uses photons in the energy range of $10 - 150eV$[42]. The general process is the following: a photon hits a material and, if the photon energy is equal or higher than one the orbital states, an electron can be ejected[43]. Due to the photon energy range, this technique is surface sensitive and allows to obtain a great description of the valence band, which makes it suitable for studying catalytic active materials like $\gamma - Al_2O_3$[6]. Another important features are that, UPS is a non-destructive technique that is suitable for conductor or semiconductor materials. Nevertheless, insulator samples can also be studied if previous preparation is made to avoid charging. Additionally, this technique needs ultra-high vacuum conditions and a spectrum analyzer. For experiments, the most common photon source is the He discharge lamp with resonance lines at $21.2eV$ and $40.8eV$[42].

To perform the simulation, it is important to understand the theoretical aspects of this effect. The probability for an electron to be ejected from the surface is related to the energy of the incident photon, the photoionization cross-section, and the material composition itself[44]. The main equation behind the working principle is Eq. 2.27[42], where the kinetic energy E_{kin} of the ejected electrons is related to the photon energy $\hbar\omega$, the binding energy E_{bin}

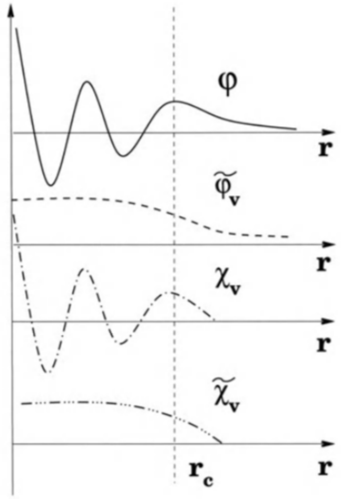

Figure 2.3: Graphical description of Eq.2.26 that describes the mechanism of the PAW pseudopotential. Taken from ref.[3]

and the workfunction of the material Φ. Thus, this technique is also very useful since it allows to calculate the workfunction that can help in the validation of simulations and general characterization of the material[45]. The last aspect to be addressed for this technique is the concept of the Inelastic Mean Free Path (IMFP), which is the distance from which the electrons will be ejected from the surface, as a result of the interaction with incident photons of a specific energy. The IMFP becomes useful to acquire experimental or simulation spectra to study the outermost layers[4]. In Fig. 2.4 (taken from ref.[4]), it is shown an example of the relation of the IMFP with the photon energy. If for a particular material, the photons of interest have an energy of $50eV$ approximately, then they will penetrate the sample up to a distance of around 6Å. In general, for the simulations it is going to be used the Density of states (DOS), the IMFP and the photon-cross section probabilities taken from ref.[7]

$$E_{kin} = \hbar\omega - E_{bin} - \Phi \tag{2.27}$$

2.3 Surface Energy

The surface energy is an important thermodynamic parameter, since it allows to determine the most stable configurations. It is a measure of the cost of increasing the surface area or the excess energy due to breaking bonds[46,47]. This parameter will be used in this work to determine best configurations for each model, that will be in principle, the surfaces with the lowest energy values, that are more likely to appear in nature. Also, the surface energy calculation will be performed for both stoichiometric and non-stoichiometric surfaces.

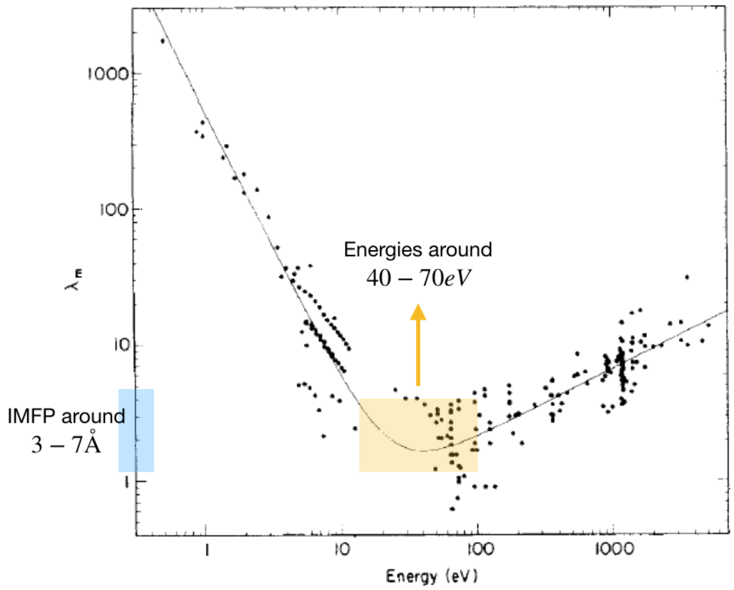

Figure 2.4: Adapted from ref.[4]. The figure shows the IMFP of a sample where the y axis is in Å. The yellow region correspond to energies around $40 - 70eV$, that are related to IMFP of around $3 - 7Å$. This means that for this energy range, the photons will penetrate that distance into the surface

2.3.1 Stoichiometric surfaces

In the case of stoichiometric surfaces, Eq. 2.28, it is used to calculate the surface energy. Here, A, E_{slab} and N, are the area, the energy obtained from the calculations and the number of atoms in the system. The term E_{bulk} is the energy of the bulk structure. A common approach to ensure that a surface has the proper thickness, meaning the atoms at the top perceive the rest of the atoms as if they were part of the bulk structure, is following the approach done in refs.[24,48]. The Eq. 2.29, is a linear relation between the energy obtained from the calculations and the number of atoms (N). Therefore, for a particular surface it is possible to try configurations varying the thickness that will have different number of atoms and calculate the energy (E_{slab}) for each of them. Then, this data (E_{slab} vs. N) can be fitted with Eq. 2.29 and the slope should yield the energy of the bulk structure.

$$\sigma = \frac{1}{A} \lim_{N \to \infty} \frac{1}{2}(E_{slab}^{N} - NE_{bulk}) \tag{2.28}$$

$$E_{slab} \approx 2A\sigma + NE_{bulk} \tag{2.29}$$

2.3.2 Non-stoichiometric surfaces

The study of non-stoichiometric surfaces is really useful to relate DFT simulations with high pressure applications (e.g. catalysis)[49]. The surface energy for the non-stoichiometric case was calculated using the formalism provided by ref.[49]. If we consider a surface oxide with chemical formula M_xO_y, where M is any metal. This surface is in contact with an oxygen atmosphere at a certain pressure (p) and temperature (T), and the environment can give or take O atoms from the surface.
In this scenario, the appropriate thermodynamic potential to describe the energy involved in this process is the Gibbs Free Energy $G(T, p, N_M, N_O)$ which is given by Eq. 2.30[50]. Here, G^{slab} refers to the total energy of a system obtained from self-consistent calculations. The value of G will also depend on the number of atoms of M and O (N_M, N_O), and the chemical potential μ_i, where the index $i = M, O$. The remaining term is the vibrational contribution ΔG^{vib}, which can be neglected, as it has been proved in previous works with metal oxides[51],[49].

$$G = G^{slab} + \Delta G^{vib} - \sum N_i \mu_i(T, p) \tag{2.30}$$

Therefore, considering the surface energy per unit area γ, it is obtained Eq. 2.31. The pre-factor $1/2$ it is used to account for the fact that when modelling surfaces, there are two equivalent faces. In this case, the chemical potentials are related by Eq. 2.32[49]. Finally, using Eqs. 2.31 and 2.32 it is possible to obtain the γ expression for, $\gamma - Al_2O_3$. In this case, $M = Al, x = 2$ and $y = 3$, that result in Eq. 2.33, and is going to be used for the calculations in this work. In principle, it is going to be observed the dependence of γ with respect to changes in μ_O

$$\gamma(T, p) = \frac{1}{2A}\left[G^{slab}(T, p, N_M, N_O) - N_M\mu_M(T, p) - N_O\mu_O(T, p)\right] \tag{2.31}$$

$$x\mu_M(T, p) + y\mu_O(T, p) = g^{bulk}_{M_xO_y}(T, p) \tag{2.32}$$

$$\gamma(T, p) = \frac{1}{2A}\left[G^{slab}(T, p, N_{Al}, N_O) - \frac{N_{Al}}{2} g^{bulk}_{Al_2O_3} + \left(\frac{3}{2}N_{Al} - N_O\right)\mu_O\right] \tag{2.33}$$

Now, it is possible to associate the surface energy results with specific T and p conditions, using the expression for μ given by Eq.2.34[49], where p^o is the pressure at normal conditions. In ref.[52], it is possible to find the data that contains the value of $\mu_O(T, p^o)$ for different temperatures. Therefore, it is possible to relate $\mu_O(T, p)$ to a range of pressures at a specific temperature. It is important to mention that this relation is done by setting a zero reference state as the half of the total energy of an isolated oxygen molecule($\mu_O(0K, p) = 1/2E^{total}_{O_2} = 0$)[49]

$$\mu_O(T, p) = \mu_O(T, p^o) + 1/2kT \ln \frac{p}{p^o} \tag{2.34}$$

Chapter 3

Computational Method

The calculations were done using Vienna *ab initio* Simulation Package (VASP)[53] under the strongly constrained and appropriately normed (SCAN) meta generalized gradient approximation (GGA). In the following section, I am going to give an overview of VASP characteristics to perform computational modelling of crystals. The general process is to start from the optimized bulk structure of a material to model different surface planes. The results in this work were achieved by choosing parameters that allow to have an energy convergence of $1 meV/atom$[54]. The computations are going to be static and structural relaxation calculations, where the ions are allowed to move considering the internal stress effect. The relaxation is done until the internal forces felt by the ions is less than $0.02 eV/\text{Å}$.

3.1 VASP

VASP is a code to perform DFT calculations that uses an atom-independant basis set of wave functions to solve the Khon-Sham equations. For this reason, it is ideal to simulate crystalline systems. Additionally, it uses pseudopotentials for the core electrons. In this work, the Projector Augmented Wave (PAW) potentials are used for the electronic configuration in Al ($[Ne]3s^2 3p^1$) and O ($[He]2s^2 2p^4$). To run a VASP simulation you need four input files: INCAR, where all the simulations parameters are included depending on which properties you want to consider; POSCAR, that contains the atomic positions and reciprocal lattice vectors; KPOINTS, where it is specified the k-points grid of the system; and finally the POTCAR, that has the pseudopotentials of the atoms involved in the calculations, in the same order as they appear in the POSCAR file. VASP uses the pseudopotential formalism explained in Section 2.1.5.

3.2 Bulk system

These simulations require the use of a plane-wave basis set, which in theory is an infinite sum over wave vectors. However, for practical purposes it is necessary to define a maximum number of plane waves that are going to be used in the calculations. In VASP, this parameter is set with the ENCUT tag in the INCAR file, which is the energy associated to the wave vector in the reciprocal space. Therefore, the first step in the simulation of the bulk structure is to find the minimum value of ENCUT that can be used, that will be related to the ground state wave function. For this, it is necessary to calculate the total energy of the system using different ENCUT values to determine at which point we observed a behaviour with the desired convergence.

Once the ENCUT energy is found, then is necessary to focus in the grid of k-points ($M \times N \times K$), since most of the integrals in DFT are evaluated in the reciprocal space. Since the reciprocal space is continuous, it is important to use accurate methods to discretize this space to get the minimum number for irreducible k-points, by finding the proper distance $\Delta_k(\text{Å}^{-1})$, in which the space is going to be divided. One of the most common procedures to do this k-points sampling is the Monkhorst-Pack[55] method with the improvements of the Moreno-Soler approach[56]. Then, as the previous step, the total energy needs to be calculated with respect to the k-points grid, to choose the proper Δ_k at which the system reaches convergence.

Now that we have the proper ENCUT energy and k-points grid, it is possible to optimize the bulk structure volume. The previous processes were done only with static calculations, but now the INCAR file will be set to allow the structural relaxation of the systems with the conditions mentioned before. Also, before the actual relaxation occurs, a rapid relaxation with a lower ENCUT energy and k-points grid, will be performed to help in the convergence process. In this part, the total energy is calculated using different cell volumes. The resulting data is fitted with the Birch-Murnaghan Equation of State[57] (Eq. 3.1) that can relate the energy with the volume. Here, E_o, V_o, B_o and $B_o^{'}$ are the ground state energy and volume, the bulk modulus, and the bulk modulus derivative, respectively. Using the data from the calculation, it is possible to find these parameters. In particular, V_o will be the optimal volume of the system, that can be found by applying the condition that it should minimize the energy ($dE(V)/dV = 0$). Additionally, the Bulk modulus can be found with the Eq. 3.2.

$$E(V) = E_o + \frac{9V_oB_o}{16}\left\{\left[\left(\frac{V_o}{V}\right)^{2/3} - 1\right]B_o^{'} + \left[\left(\frac{V_o}{V}\right)^{2/3} - 1\right]^2\left[6 - 4\left(\frac{V_o}{V}\right)^{2/3}\right]\right\} \tag{3.1}$$

$$B_o = V_o\frac{\partial^2 E(V)}{\partial V^2} \tag{3.2}$$

3.3 Surfaces

From the optimized Bulk structure, it is possible to construct surfaces by cutting the system at different crystallographic planes. Surfaces are only periodic in two directions (x and y). Thus, to model these systems in VASP, that considers periodicity in all directions, it is necessary to consider a slab surface that impose a separation (vacuum) between images in the z axis, and allow to neglect the interaction in this direction. In this work it was used a vacuum slab of 15Å. Additionally, dipole corrections are necessary to be considered in surfaces modeling and this can be done by writing the tag IDIPOL = 3 in the INCAR file. Also, the KPOINTS file has to be modified taking account that a new grid will be used since the cell dimensions have changed. For the surfaces, the grid if k-points is in the form of $M \times N \times 1$. Additionally, the treatment with Eq. 2.29, is used to define the proper thickness of the surfaces. After these considerations, the static and structural relaxations can be performed in the surface systems.

For experimentalists, it is generally easier to consider results in a cubic system. That is why, for our Models, we are going to consider miller planes, whose equivalent planes in the cubic system, might be of relevance. The idea is that if we want to study the plane (*xyz*) in the cubic system, we have to take the models, which have non-cubic symmetries, and find the planes (*abc*) that are equivalent to (*xyz*), by analyzing our models as if they would actually have cubic symmetries. Finally, once we find the proper (*abc*) planes, we use these them to cleavage the bulk structure and get a surface. Using this idea, the miller planes of interest in the cubic system (due to their appearance in the literature) are (111), (001) and (110). These planes correspond to the (010), $(1\bar{1}0)$ and (001) for the symmetry in M1, respectively. For the symmetry in M2, the equivalent planes are (032), (001) and (100), respectively. It is important to state that these equivalences are being made with respect to a perfect cubic spinel system. In Fig. 3.1 it is displayed an example of how to get this equivalence. As it is observed in Fig. 3.1a, it shows the (111) surface of a perfect cubic spinel system for the material (no defects), where appears a characteristic hexagonal form. In Fig. 3.1b, it is observed the system M1, showing the surface (010), where it can also be distinguished the hexagonal forms, therefore, it is possible to say that these two surfaces are equivalent. Finally, the same situation it is shown in Fig. 3.1c, where the surface (032) contains the familiar hexagonal forms. This is the general procedure to get the surface planes. From now on, we are only going to refer to the planes in the cubic system for simplification.

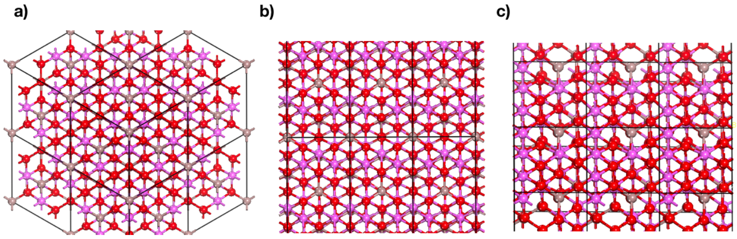

Figure 3.1: **(a)** Perfect cubic spinel system showing the (111) surface plane. **(b)** Defective spinel system (M1) showing the (010) surface plane which shows equivalent atomic organization as in (a). **(c)** Non-defective spinel system (M2) showing the (032) surface plane which shows equivalent atomic organization as in (a)

Different reconstructions appear for each direction as a result of getting all the possible stoichiometric surfaces. After obtaining the total energy of each surface, the surface energy σ was calculated to determine which are the most energetically-favorable surfaces. Using the most stable surfaces in each model, non-stoichiometric surfaces were also constructed and their stability was analyzed using Eq. 2.33.

UPS spectra and the workfunctions were simulated for the main cases in stoichiometric systems. For the workfunction, the local potential was calculated without considering exchange-correlation potential ($V_{XC}(\vec{r})$) and it was saved in an output VASP file called LOCPOT. This is done by setting the tag LVHAR = T in the INCAR file. The Inelastic Mean Free Path (IMFP) considered for this material is 7Å and it was obtained using NIST Electron Inelastic-Mean-Free-Path Database[5], with a photon energy of $50eV$. This is a software that allows to predict the IMFP from inorganic compounds using Eq. 3.3, that was developed in the work described in ref.[58]. In this equation,

λ is the IMFP (Å), E is the electron energy (eV), E_p is the free-electron plasmon energy (eV), ρ is the density (g/cm^3), N_v is the number of valence electrons per molecule, M is the molecular weight and E_g is the band gap energy (eV). In Fig. 3.2, it is shown the steps to follow in the software. First, in the tool Database→Inorganic compounds, we have to choose **IMFPs from predictive formula**. Then, we select the elements involved. After that, we provide the materials properties that appear in Eq. 3.3. Finally, we will obtain a plot of the IMFP as a function of the energy.

$$\lambda = \frac{E}{E_p^2[\beta \ln(\gamma E) - (C/E) + (D/E)^2]} \tag{3.3}$$

$$E_p = 28.8(N_v\rho/M)^{1/2}$$

$$\beta = -0.0216 + 0.944/(E_p^2 + E_g^2)^{1/2}$$

$$\gamma = 0.191\rho^{-0.5}$$

$$C = 1.97 - 0.91U$$

$$D = 53.4 - 28.8U$$

$$U = N_v\rho/M = E_p^2/829.4$$

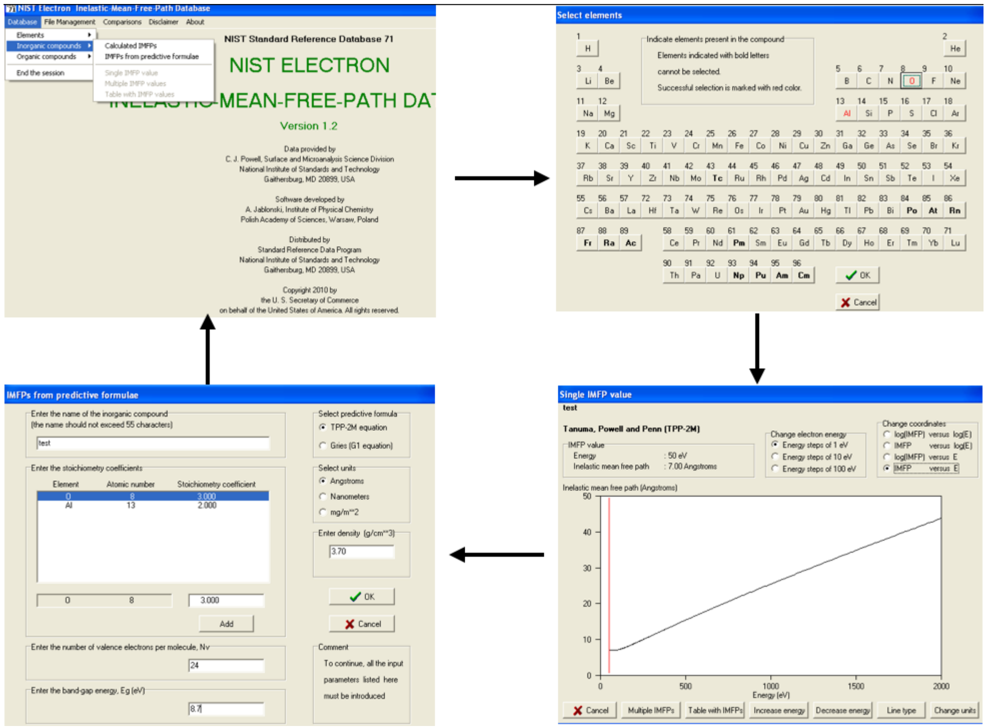
NIST Electron Inelastic-Mean-Free-Path Database
Database
File Management
Comparisons
Disclaimer
About
Elements
Inorganic compounds
Organic compounds
End the session
Calculated IMFPs
IMFPs from predictive formulae
Single IMFP value
Multiple IMFP values
Table with IMFP values
Select elements
OK
Cancel
Add
Multiple IMFPs
Table with IMFPs
Increase energy
Decrease energy
Line type
Change units
Inelastic mean free path (Angstroms)
Energy (eV)
0
10
20
30
40
50
500
1000
1500
2000

NIST Standard Reference Database 71

NIST ELECTRON

INELASTIC-MEAN-FREE-PATH DATA

Version 1.2

Data provided by
C. J. Powell, Surface and Microanalysis Science Division
National Institute of Standards and Technology
Gaithersburg, MD 20899, USA

Software developed by
A. Jablonski, Institute of Physical Chemistry
Polish Academy of Sciences, Warsaw, Poland

Distributed by
Standard Reference Data Program
National Institute of Standards and Technology
Gaithersburg, MD 20899, USA

Copyright 2010 by
the U. S. Secretary of Commerce
on behalf of the United States of America. All rights reserved.

Indicate elements present in the compound
Elements indicated with bold letters cannot be selected.
Successful selection is marked with red color.

IMFPs from predictive formulae

Enter the name of the inorganic compound (the name should not exceed 55 characters): test

Enter the stoichiometry coefficients

Element	Atomic number	Stoichiometry coefficient
O	8	3.000
Al	13	2.000

Enter the number of valence electrons per molecule, Nv: 24

Enter the band-gap energy, Eg (eV): 8.7

Select predictive formula: ● TPP-2M equation ○ Gries (G1 equation)

Select units: ● Angstroms ○ Nanometers ○ mg/m**2

Enter density (g/cm**3): 3.70

Comment: To continue, all the input parameters listed here must be introduced

Single IMFP value

test

Tanuma, Powell and Penn (TPP-2M)

IMFP value
Energy : 50 eV
Inelastic mean free path : 7.00 Angstroms

Change electron energy: ● Energy steps of 1 eV ○ Energy steps of 10 eV ○ Energy steps of 100 eV

Change coordinates: ○ log(IMFP) versus log(E) ○ IMFP versus log(E) ○ log(IMFP) versus E ● IMFP versus E

Figure 3.2: General view of the NIST Electron Inelastic-Mean-Free-Path Database[5]. Starting from the upper left side, the images show the steps to get the IMFP from inorganic compounds using the predictive formula (Eq. 3.3)

Chapter 4

Results & Discussion

4.1 Bulk structure

4.1.1 Model 1 (M1)

In the Methodology section, it was mentioned the general procedure to perform the optimization for the bulk systems. In Fig. 4.1, it is shown the results of the ENCUT energy and KPOINTS analysis for M1. It was obtained an ENCUT value of $750eV$ and a $\Delta_k = 0.040\text{Å}^{-1}$ that corresponds to a $5x5x2$ mesh, which are the parameters that allow a total energy convergence of $1meV/atom$. The next step was to calculate the optimal cell volume by performing a structural relaxation in the system and calculating the total energy varying the unit cell volume. After that, the data was fitted using Eq. 3.1 (Fig. 4.2) to get the optimized volume that corresponds to the ground state system.

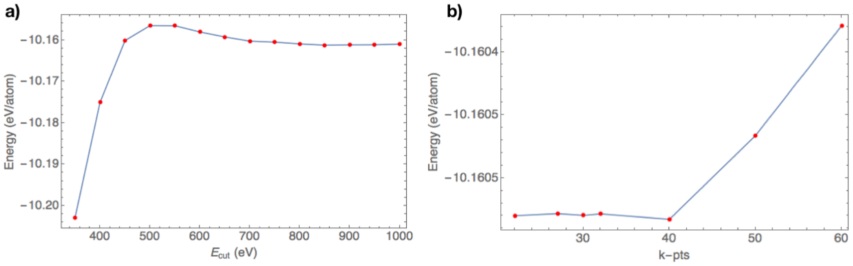

Figure 4.1: Results of the static calculations in M1 for the **(a)** Total Energy vs. ENCUT energy and **(b)** Total Energy vs. KPOINTS computations

The bulk structure for the Model 1 used in this work is displayed in Fig. 4.3, where the indexes A and B correspond to tetrahedral and octahedral sites, and the letter V is used to label the vacancies in the octahedral sites. From the results of the relaxation, it was possible to get relevant parameters like the optimal cell volume ($V_o = 365.986\text{Å}^3$), lattice parameters and Bulk modulus ($B_o = 219GPa$), which is higher than the one reported

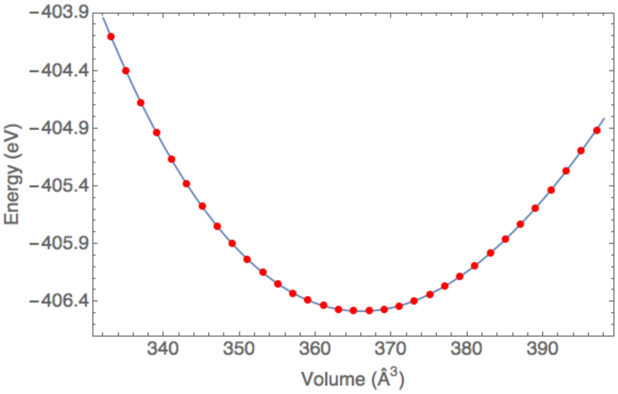

Figure 4.2: Data for the Total Energy calculations with respect to the cell volume (red dots) and the fitting with the Birch-Murnaghan Equation of State (blue solid line) for M1.

in ref.[24]. This information is summarized in Table 4.1, that contains the crystallographic data for Model 1. The lattice parameter in the cubic system obtained with this functional is 7.87Å, which is lower than the one reported by Pinto[24], but much closer to the experimental value reported in ref.[59](7.88Å). The Table 4.1 shows the fractional coordinates of sites u, w and w, including the location of the vacancies ($V_{\rm 1B}$, $V_{\rm 2B}$). It was also obtained the electronic structure for M1 (Fig. 4.4), where is observed an insulating behaviour as it is expected. The band gap energy for M1 is E_g^{M1} = 4.9 eV.

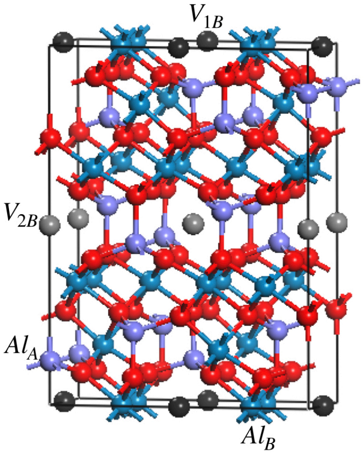

Figure 4.3: Defective spinel bulk system for Model 1 (M1). The tetrahedal Al_A, and octahedral Al_B atoms are represented in purple and blue, respectively. The vacancies are represented with black and grey spheres and the O atoms are the red spheres.

Table 4.1: Crystallographic data of $\gamma - Al_2O_3$ for Model 1.

Property	Calculated		
Space group	$C2/m$		
$a = b$(Å)	5.5803		
c/a	2.4224		
$\alpha = \beta(^o)$	90.5		
$\gamma(^o)$	60.401		
Volume (Å^3)	365.986		
B$_o(GPa)$	219		
Sites	u	v	w
Al(1)$_\mathrm{A}$	0.3239	0.3239	-0.7925
Al(2)$_\mathrm{A}$	0.0020	0.0020	-0.8777
Al(3)$_\mathrm{A}$	0.6677	0.6677	-0.4530
Al(4)$_\mathrm{B}$	0.6772	0.1662	-0.3400
Al(5)$_\mathrm{B}$	0.6514	0.6514	-0.8397
Al(6)$_\mathrm{B}$	0.1672	0.1672	-0.3389
Al(7)$_\mathrm{B}$	0.0000	0.5000	0.0000
O(1)	0.8446	0.3456	-0.9138
O(2)	0.4902	0.0326	-0.2545
O(3)	0.8377	0.3332	-0.4061
O(4)	0.8224	0.8224	-0.9164
O(5)	0.6793	0.6793	-0.0793
O(6)	0.4951	0.4951	-0.2526
O(7)	0.8368	0.8368	-0.4062
O(8)	0.3368	0.3368	-0.4125
O(9)	0.0045	0.0045	-0.2582
V$_\mathrm{1B}$	0	0	0.5
V$_\mathrm{2B}$	0.5	0.5	0

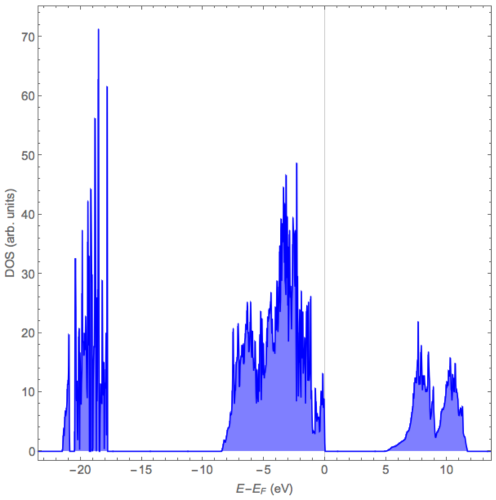

Figure 4.4: SCAN computed DOS for system M1. The line represents the Fermi level at zero and it is observed a bandgap of $E_g^{M1} = 4.9$ eV

4.1.2 Model 2 (M2)

In the case of M2, it is observed in Fig. 4.5, the results of the ENCUT energy and KPOINTS analysis. It was obtained an ENCUT value of $750eV$ and a $\Delta_k = 0.040\text{Å}^{-1}$ that corresponds to a $4x3x3$ mesh, which are the parameters that allow a total energy convergence of $1meV/atom$. The ENCUT energy and Δ_k is the same as in M1 and it is probably related with the fact that both systems are really similar. To get the optimal cell volume, it was used again Eq. 3.1 to fit data after the structural relaxation (Fig. 4.6)

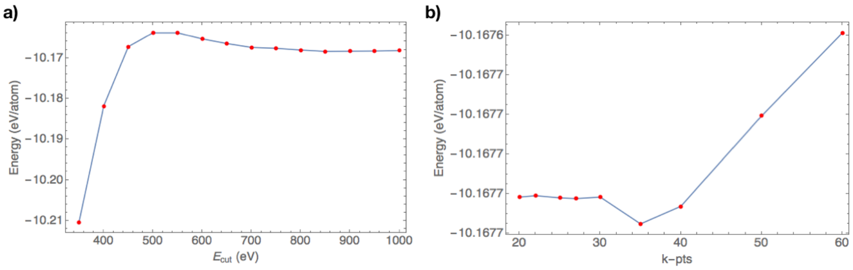

Figure 4.5: Results of the static calculations in M2 for the **(a)** Total Energy vs. ENCUT energy and **(b)** Total Energy vs. KPOINTS computations

In Fig. 4.7 it is observed the bulk structure for M2, which is a cubic system without vacancies. For this case, the optimal cell volume ($V_o = 364.777$ Å^3) and Bulk modulus ($B_o = 200$ GPa), which is higher than the value reported in ref.[15]. The crystallographic information is summarized in Table 4.2. The Density of States calculated for this

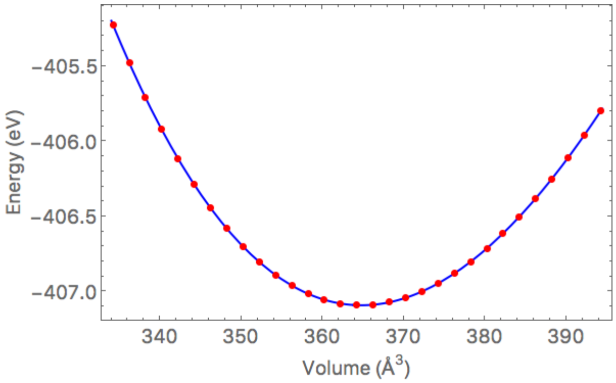

Figure 4.6: Data for the Total Energy calculations with respect to the cell volume (red dots) and the fitting with the Birch-Murnaghan Equation of State (blue solid line) for M2.

system also shows an insulating behaviour as it is observed in Fig. 4.8. The bandgap energy for M2 is $E_g^{M2} = 5.79eV$. It is important to remark that the bandgaps for both models calculated with the SCAN functional are closer to the experimental value ($E_g^{M2} = 8.7eV$[60]) as compared to the previous calculations with GGA functional[24, 15].

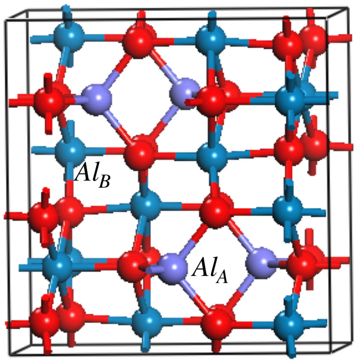

Figure 4.7: Non-defective spinel bulk system for Model 2 (M2). The tetrahedal Al_A, and octahedral Al_B atoms are represented in purple and blue, respectively. The O atoms are the red spheres.

4.2 Surfaces

4.2.1 Stoichiometric surfaces

In this section, it is going to be shown stoichiometric surfaces for three different planes. For each plane, the results for both models are going to be compared. The arrows in the Figures represent the movement of the atoms when

Table 4.2: Crystallographic data of $\gamma - Al_2O_3$ for Model 2.

Property		Calculated	
Space group		$P21/M$	
a(Å)		5.5089	
b(Å)		8.2933	
c(Å)		7.9846	
$\alpha = \gamma(^o)$		90.0	
$\beta(^o)$		90.5	
Volume (Å^3)		364.777	
B$_o(GPa)$		200	
Sites	u	v	w
Al(1)$_\mathrm{A}$	0.6169	0.7500	0.7464
Al(2)$_\mathrm{A}$	0.8688	0.2500	0.4996
Al(3)$_\mathrm{B}$	0.3676	0.0754	0.6132
Al(4)$_\mathrm{B}$	0.1177	0.5784	0.8629
Al(5)$_\mathrm{B}$	0.3781	0.7500	0.1258
Al(6)$_\mathrm{B}$	0.8759	0.7500	0.1252
O(1)	0.8874	0.4061	0.8980
O(2)	0.6062	0.9179	0.6139
O(3)	0.3574	0.4061	0.8543
O(4)	0.1364	0.9168	0.6370
O(5)	0.8833	0.7500	0.8769
O(6)	0.3628	0.7500	0.8898
O(7)	0.6123	0.2500	0.6404
O(8)	0.1338	0.2500	0.6284

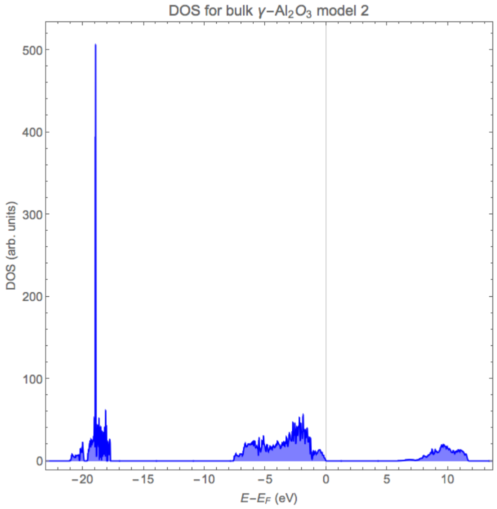

Figure 4.8: SCAN computed DOS for system M1. The line represents the Fermi level at zero and it is observed a bandgap of E_g^{M1} = 4.9 eV

passing from an un-relaxed to a relaxed state.

Surface (111)

For M1, the plane (010) of the system was cleavage to get the surface that is equivalent to the (111) plane in the cubic system. To maintain an stoichiometric surface it was observed that there were two possible reconstructions that were labeled as (111)*a* and (111)*b*, and differ in the coordination of the top Al atom. In Figs. 4.9 and 4.10 are shown the side and top view of the surfaces (111)*a* and (111)*b*, respectively. For the first one, the terminations are tetrahedral Al atoms, while for the latter, the top Al atoms occupy octahedral sites. In the relaxed (111)*a* surface, the Al_A moves down while the surrounding oxygens (see Fig. 4.9 b) move up in z direction. The oxygen closer to the Al_B atoms in Fig. 4.9 b also moves down as the arrows are indicating. The oxygens in the top-most layer of surface (111)*b* behave in a similar way after relaxation, as it is observed in Fig. 4.10a,b, but now the Al_B atom at the top is the one that moves down.

On the other hand, for M2 the first surface slab is the plane (032) that is also equivalent to the (111) plane in the cubic system. In Fig. 4.11, it is observed the side view of this surface, where it is clear that the top layer consists of a mixture of Al_A and Al_B atoms, in sort of a combination of the (111) reconstructions in M1. After relaxation, most of the atoms in the top layer move down, except for one oxygen that moves approximately 1.8Å in the z direction. This oxygen at the top is forming a small lump at the surface. It is also noticeable that the there is a region in the top layers, where a kind of an amorphous phase is formed, while the middle zone short range order is maintained. Another important point is that this re-ordering of the atoms after relaxation, is not observed in ultra-thin films (≈ 9Å), but it starts to appear in thicker films (≈ 16.9Å). In the work done by Digne, *et. al*[15], they studied this

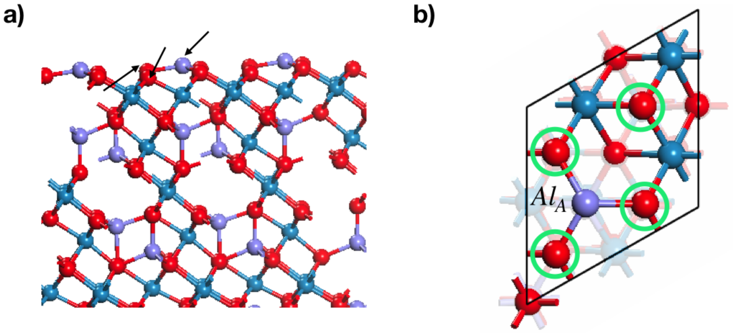

Figure 4.9: **(a)** Side and **(b)** top view of surface (111)a for M1. The circles in part (b) correspond with the atoms with arrows in part (a)

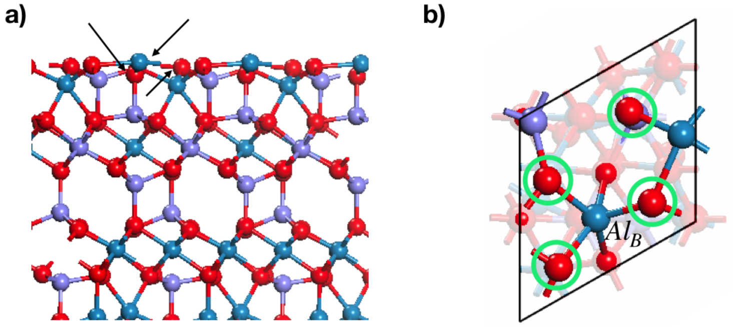

Figure 4.10: **(a)** Side and **(b)** top view of surface (111)b for M1. The circles in part (b) correspond with the atoms with arrows in part (a)

surface and obtained a similar result of stacking of O and Al atoms, and some of the amorphous reconfiguration is observed. However, they did not study thicker films to observe the reconstruction observed in this work.

Surface (001)

For M1, The surface (001) in the cubic system is obtained by cutting the bulk structure in $(1\bar{1}0)$ plane. The surfaces reconstructions are called $(001)a$ and $(001)b$ and their side views are shown in Fig. 4.12. After structural relaxation, in the surface $(001)a$ most of the Al atoms at the top move down, with the exception of two Al_A atoms that move up (Fig. 4.12a); while in surface $(001)b$ we get a very similar behaviour, but the Al_A atoms that move up are located at different zones, and the top-most Al_A atom maintains a constant position in z direction.

In the case of M2, the plane (001) was used to get (001) surface in the cubic system. There are also two reconstructions $(001)a$ and $(001)b$ (see Fig. 4.13) that differ because of the difference in position of the layer that contains the characteristic rhombus formed by Al_A atoms. The surface $(001)a$ presents this layer at the top, while in

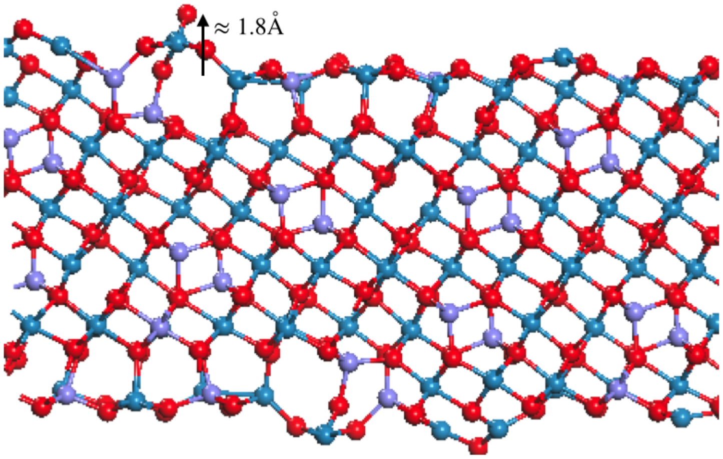

Figure 4.11: Surface (111)b plane for M2

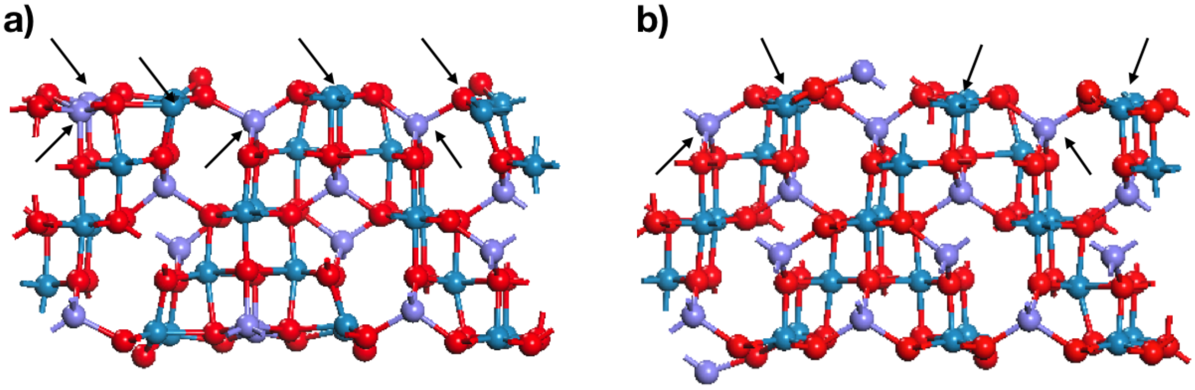

Figure 4.12: Side view of the surfaces **(a)** (001)a and **(b)** (001)b for M1.

surface (001)*b* it is the middle. After relaxation, in the surface (001)*a* most of the atoms at the top remain unchanged with the exception of an Al_A atom that moves down while the two O atoms around it, move up (Fig. 4.13a). In the surface (001)*b*, all the O atoms move upwards, while the Al atoms move downwards. The Al_A atom pointed out in Fig. 4.13b has the most pronounced movement.

Surface (110)

The final surface is obtained for M1 by cleaving the (001) plane that is equivalent to the (110) plane in the cubic system. There are three reconstructions (110)*a*, (110)*b*, (110)*c* that can be observed in Fig. 4.14. In the relaxed

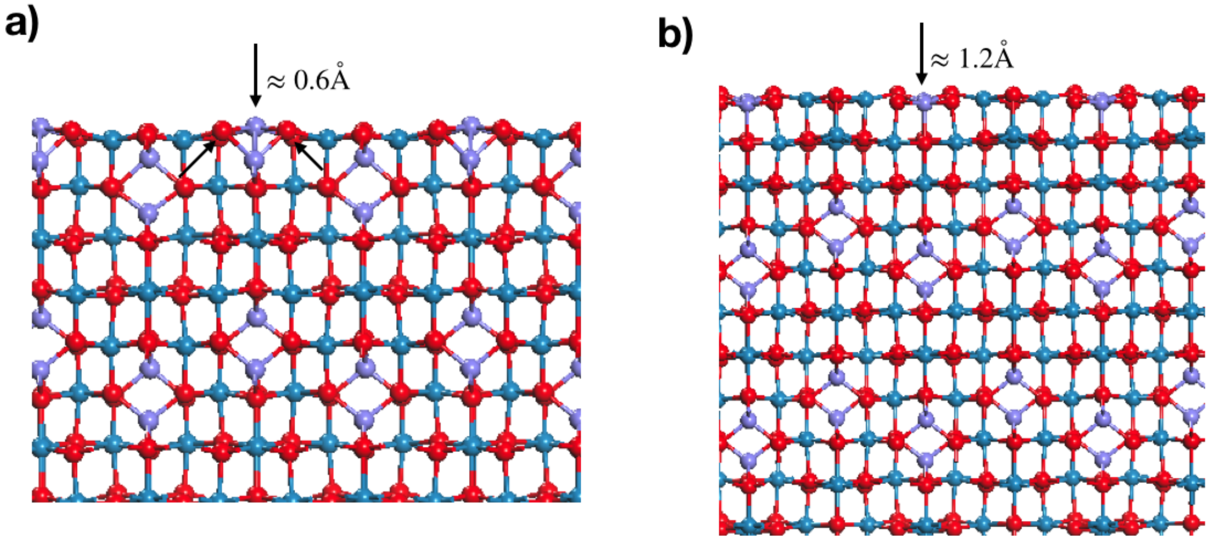

Figure 4.13: Side view of the surfaces **(a)** (001)a and **(b)** (001)b for M2.

surfaces, the Al atoms move downwards in all the cases, but the behaviour of the O atoms mark the difference. For the surface (110)*a* there are only two O that move up (Fig. 4.14a), in the surface (110)*b* most of the O atoms move up with the exception of one atom (Fig. 4.14b), finally in the surface (110)*c* the O atoms have a more pronounced displacement outwards the surface. In general, the three surfaces change by the displacement of the O atoms in the z direction. Particularly, the surface (110)*c* coincides with the surface observed by Pinto, *et al.* (2004)[24], where in the same direction they obtained a "saw-tooth surface" but only with Al_B terminations.

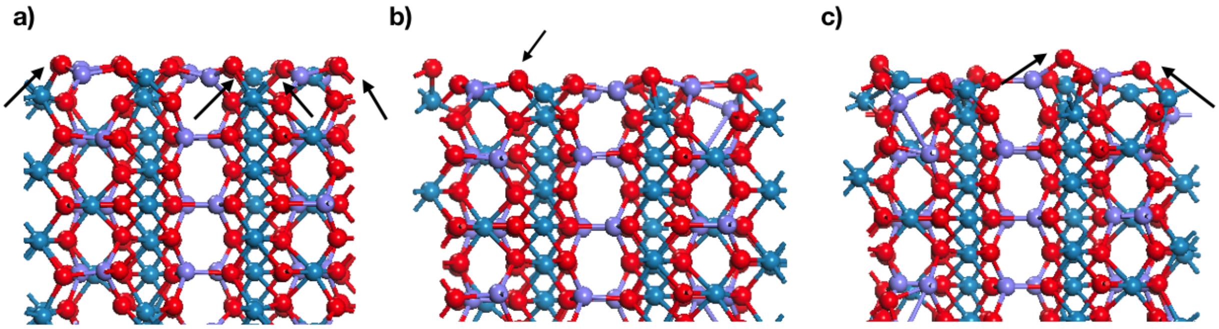

Figure 4.14: Side view of the surfaces **(a)** (110)a, **(b)** (110)b and **(c)** (110)c for M1.

For M2, the plane (100) yields the equivalent (110) surface in the cubic system. Now, there are two reconstructions (110)*a* and (110)*b*. After relaxation, all the O atoms in both reconstructions move up, but for surface (110)*a* there are two Al atoms that move down (Al_A) and up (Al_B) to get closer. On the other hand, in the surface (110)*b* all the Al atoms move down, except one Al_B that moves upwards. The same "sawtooth-like surface" it is observed for this reconstruction.

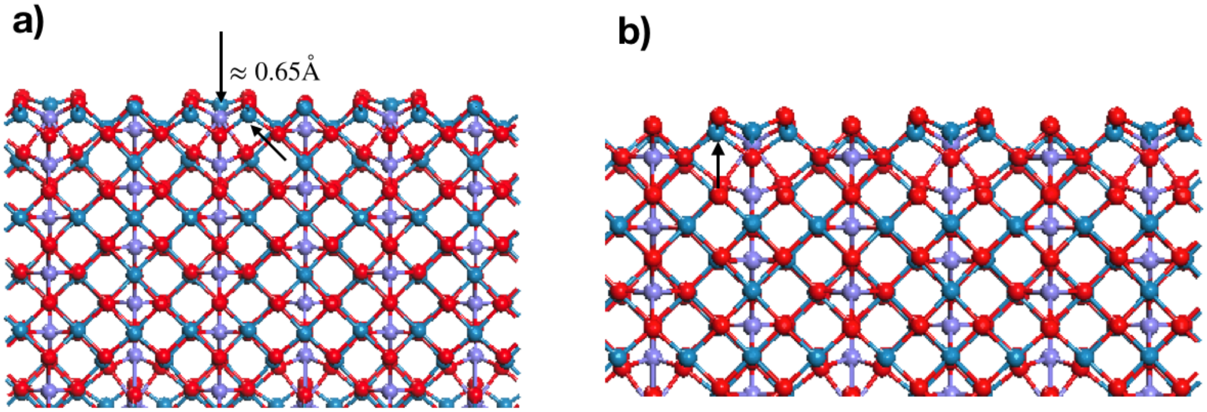

Figure 4.15: Side view of the surfaces **(a)** (110)a and **(b)** (110)b for M2.

4.2.2 Most stable surfaces

To determine the most stable configurations in each model, the surface energy was calculated for each system using Eq. 2.28. The results for M1 and M2, are shown in Tables 4.3 and 4.4, respectively. The most stable surfaces in M1 are (111)*a* and (001)*a*, with surface energy values of $79.028 meV/\text{Å}^2$ and $86.465 meV/\text{Å}^2$, respectively. For M2, the most stable surfaces are (111) and (001)*a* with a surface energy equal to $112.97 meV/\text{Å}^2$ and $118.54 meV/\text{Å}^2$, respectively.

In M1, the values of the surface energy obtained with the SCAN functional are a little bit higher than the results obtained in the work done by Pinto, *et. al*[24], but they predict the same stable surfaces. In the case of M2, the difference in surface energy of both surfaces is really small, given the fact that the values are in the order of meV. Therefore, it is possible to say that these two surfaces are equally likely to appear in nature. Additionally, the (111) surface for M2 is predicted to be more stable as the results provided by Digne, *et. al*[15].

Regarding the experimental measurement of the surface energy of $\gamma - Al_2O_3$, there are very few works that have focused on this task [61,11,62,63]. The reason is that the experimental measurement of this quantity is really challenging for solid samples[63], but the amount of theoretical works on this material state the importance of having experimental parameters to help elucidate the most stable structures[61]. In the work done by McHale (1997)[62], they obtained a value of $1.34 J/m^2$, which is really close to the value obtained for the surface (001)*a* in M1. The other works show values around $1.67 J/m^2$, that is in the middle of the surface energy of (111)a in M1 and (111) in M2.

Table 4.3: Surface energy σ calculations of the relaxed slabs in different surfaces for the cubic system of $\gamma - Al_2O_3$ in the model 1

Surfaces	N. atoms	σ (meV/Å^2)	σ (J/m^2)	E_g (eV)
(111)a	40	79.028	1.26	3.7
(111)b	40	146.916	2.35	4.2
(001)a	100	86.465	1.38	4.3
(001)b	100	132.075	2.11	3.0
(110)a	180	159.692	2.55	3.1
(110)b	180	156.726	2.51	3.2
(110)c	180	145.881	2.33	3.0

Table 4.4: Surface energy σ calculations of the relaxed slabs in different surfaces for the cubic system of $\gamma - Al_2O_3$ in the model 2

Surfaces	N. atoms	σ (meV/Å^2)	σ (J/m^2)	E_g (eV)
(111)	280	112.974	1.81	2.9
(001)a	100	118.547	1.89	4.3
(001)b	120	126.892	2.03	4.0
(110)a	120	150.660	2.41	4.0
(110)b	100	139.221	2.23	4.2

The surface energies can also help to determine the trends that the configurations follow during relaxation to reach stability. It is clear that the O atoms at the top prefer to move outwards in z direction. For the surface (111) in M1, it is observed a preference for having Al_A atoms at the top, since the (111)a surface is more stable than (111)b surface. Analyzing the case for M2, it can be said that there is a preference for planar surfaces, since (111) surface in M2, is less stable than in M1, due to the O atom that forms an abrupt lump. For the surface (001) in M1, it is observed again a preference of having Al_A at the top, but also that it is more favorable to have bare surfaces. In the case of M2, the stability is governed by the structure with a major concentration of Al_A atoms at the top. For the (110) surface in M1, the most stable surfaces are mainly governed by the presence of O atoms at the top, since Al atoms remain mostly unchanged. For M2, the most stable surface is (110)b since it has more O atom terminations rather than Al_B atoms. In general, the most stable systems are bare surfaces with preference for O and Al_A atoms.
In Figs. 4.16 and 4.17, it is displayed the Partial Density of States (PDOS) of the most stable surfaces of each Model. Likewise, the UPS spectra were simulated for these surfaces, and they are shown in Fig. 4.18 for M1, and Fig. 4.19 for M2. The main contribution to the total UPS is given by the O atoms, for each Model. In this sense, each plot

lays out the total UPS simulation and the contribution of the O atomic orbitals. It is clear that the O_{2p} orbital has the major effect in the spectra for all the cases. In the experimental work of Jiménez-González[6] for $\gamma - Al_2O_3$ thin films, it was obtained the UPS spectrum where the peak with the highest intensity corresponds to the O_{2p} that is located at $8eV$. It also appears a small shoulder at the left, and the workfunction was reported as $\phi = 2.5eV$. The overall shape of the spectrum is in agreement with our theoretical work, but the peaks were shifted to coincide with the experiment. Additionally, the shapes of the shoulders and the work functions values differ from the experiment. In Fig. 4.20, it is shown the experimental data obtained in ref.[6], where is possible to see the similarities with our theoretical work, and determine that, the UPS spectrum of the surface $(001)a - M1$ is the closest to the experiment.

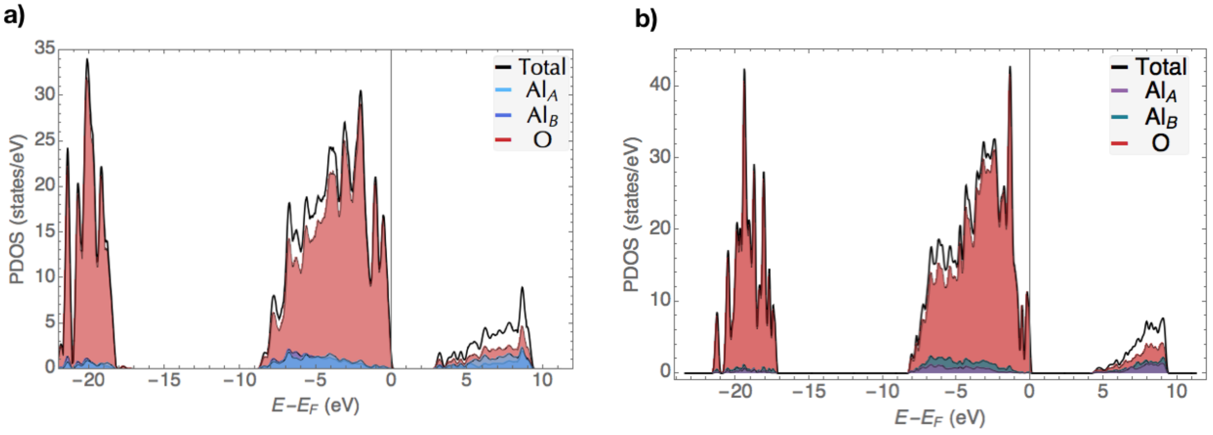

Figure 4.16: PDOS of the surfaces **(a)** $(111)a$ and **(b)** $(001)a$ of system M1. The Fermi level is represented by the line

4.2.3 Non-stoichiometric surfaces

Non-stoichiometric surfaces were derived from the most stable stoichiometric surfaces for each Model. These surfaces were obtained by removing O atoms from the top layers. For the calculation of the surface energy it was used a reference value of $E_{O_2}^{Total} = -12.34eV$

Model 1

The most stable stoichiometric surface in this model was $(111)a$. At the top layer of this surface there are two possible O vacancies. The vacancy **type a** is the removal of an O atom connected to a Al_A atoms, while vacancy **type b**, is an O atom that was connected to Al_B atoms only. Additionally, it was studied two different geometrical considerations: **trigonal (tri)**, which is the normal unit cell used previously, and the **rectangular (rec)**, which is the structure arranged in a rectangular lattice (bigger). The main difference between these two configurations is the average distance at which the vacancies will be distributed. Finally, the highlighted atoms in the figures will

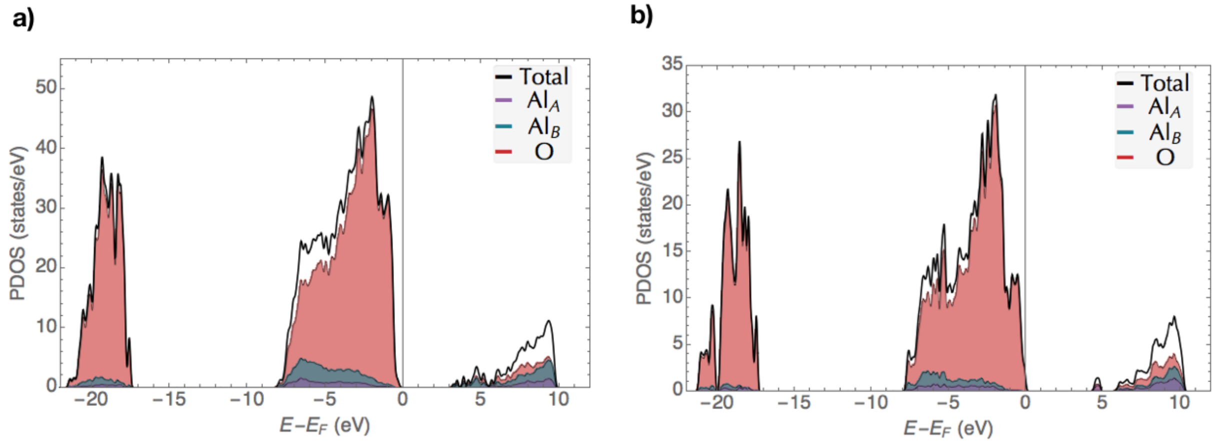

Figure 4.17: PDOS of the surfaces **(a)** (111) and **(b)** (001)*a* of system M2. The Fermi level is represented by the line

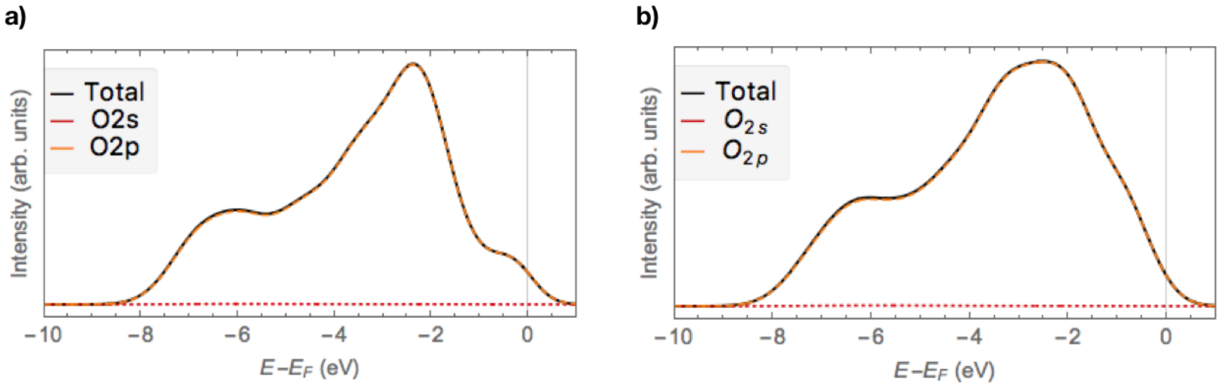

Figure 4.18: UPS of the surfaces **(a)** (111)*a* with a workfunction of $\phi = -4.7eV$ and **(b)** (001)*a* with a workfunction of $\phi = 7.7eV$ of M1 considering the atomic orbital contribution

represent the vacancies.

In Fig. 4.21, it is shown the first non-stoichiometric surfaces type a, where it is clearly observed that the O atoms that will be removed, are connected to Al_A atoms. Here, the unit cells are repeated twice in the x and y direction to get a better idea of the differences between the trigonal (Fig. 4.21 a) and rectangular (Fig. 4.21 b) configurations. On the other hand, in Fig. 4.22, it is shown the non-stoichiometric surfaces type b, where it is clearly observed that the O atoms that will be removed, are connected to Al_B atoms only.

In the previous structures, only one vacancy was considered. Now, it is going to be showed the results of removing

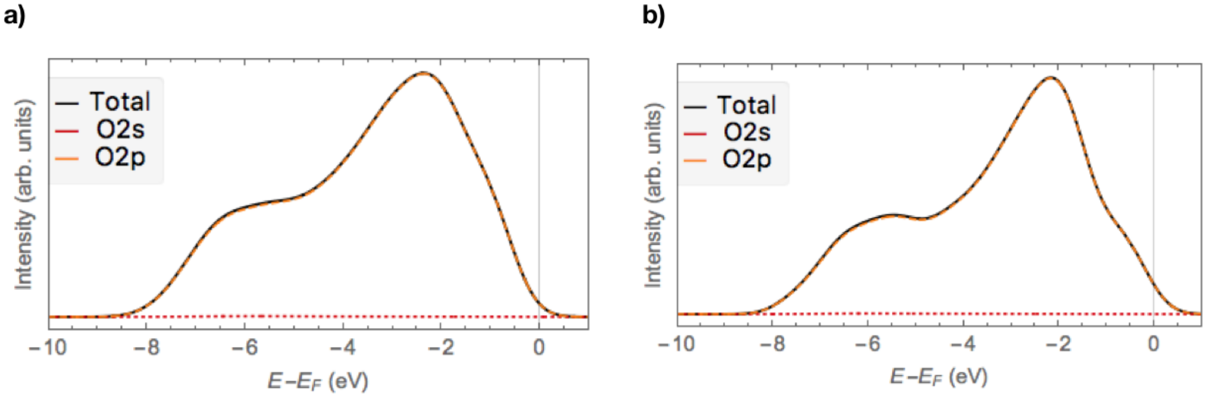

Figure 4.19: UPS of the surfaces **(a)** (111) with a workfunction of $\phi = 6.3eV$ and **(b)** (001)a with a workfunction of $\phi = 6.2eV$ of M2 considering the atomic orbital contribution

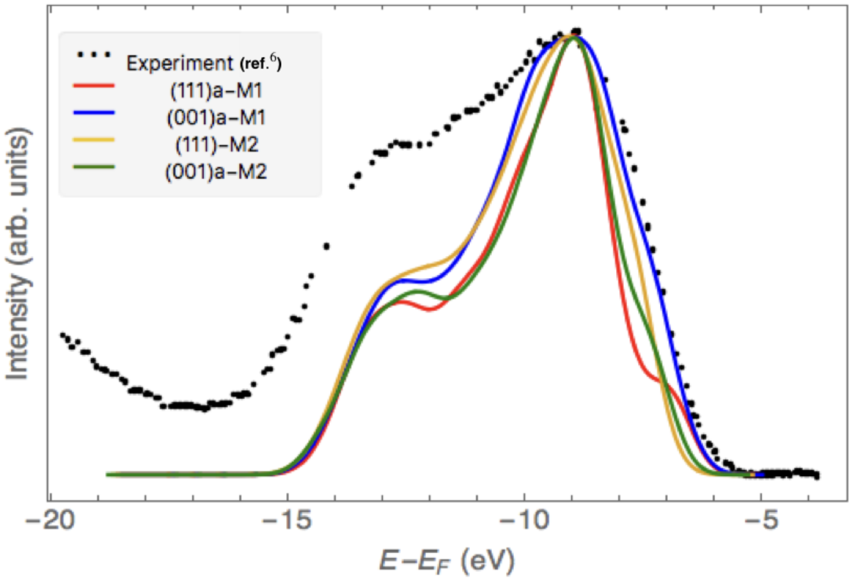

Figure 4.20: Comparison of the total UPS spectra of the most stable surfaces for Model 1 and 2 with the experimental UPS of $\gamma - Al_2O_3$ thin films obtained in ref.[6]

two O atoms. Here, the color green will represent a vacancy type a, and the color yellow, will be type b. In Fig. 4.23, it is observed the trigonal configuration of a surface where two vacancies (type a and b) have been removed.

For the case of the rectangular configuration, it was observed six different reconstructions to get a non-stoichiometric surfaces with two vacancies. In general, it was studied the case when the vacancies were equal

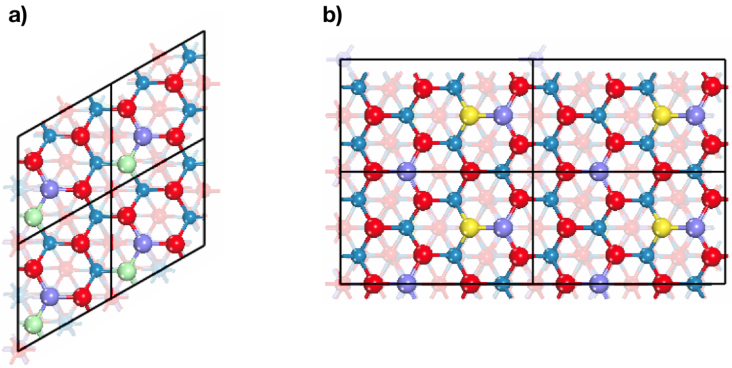

Figure 4.21: Top view of the non-stoichiometric surfaces type a in a **(a)** trigonal and **(b)** rectangular configuration. The green and yellow spheres are the vacancies type a

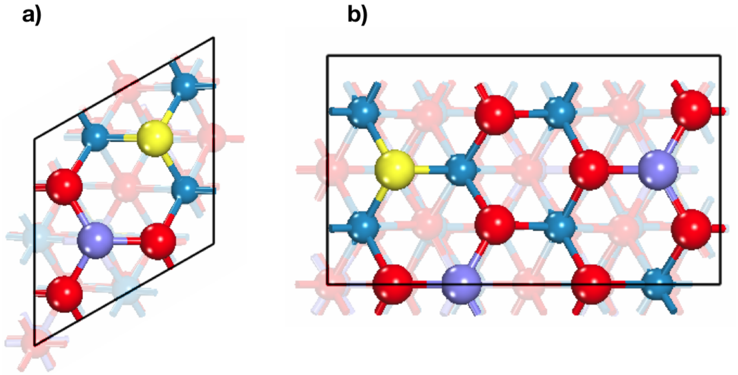

Figure 4.22: Non-stoichiometric surfaces type b in a **(a)** trigonal and **(b)** rectangular configuration. The yellow spheres represent the vacancies type b

or different. In the case of equal vacancies (Fig. 4.24), there were three possibilities: **aa**, with two vacancies type a that are far from each other, **aa2**, with two vacancies type a that are closer, and **bb**, with two vacancies type b. In the case for different vacancies (Fig. 4.25), there were also three possibilities: **ab1**, with two close vacancies in a vertical plane, **ab2**, with two vacancies in a diagonal plane, and **ab3**, with two vacancies that are further from each other.

Finally, using Eq. 2.33, it is possible to calculate the most stable configuration among these non-stoichiometric surfaces. The results are shown in Fig. 4.26, were it is associated with O atmosphere values at a specific temperature. It is observed that at these conditions of pressure and temperature, the non-stoichiometric surfaces are less stable, than the stoichiometric case (black).

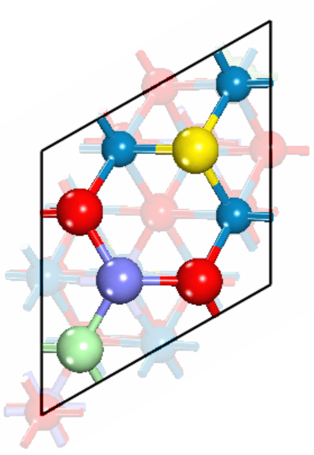

Figure 4.23: Non-stoichiometric surface type ab in the trigonal configuration. The colored spheres represent the vacancies

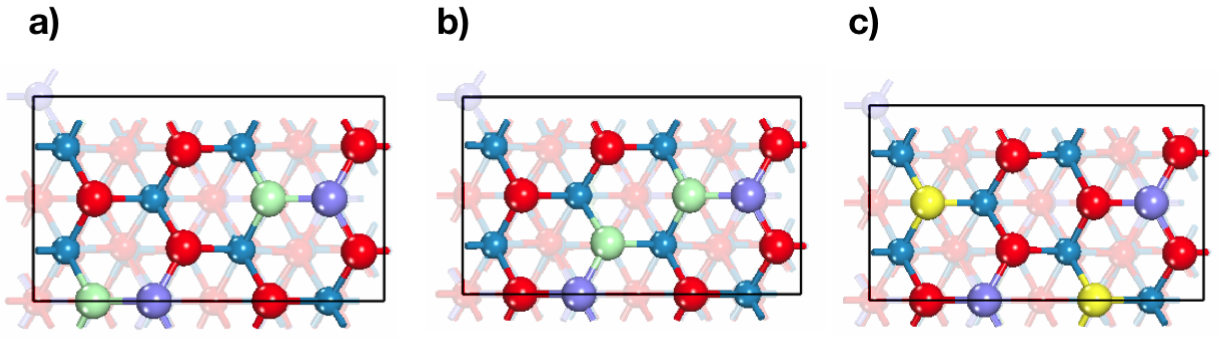

Figure 4.24: Non-stoichiometric surfaces with two vacancies of the same type, where **(a)** is the aa case, **(b)** is the aa2 case and **(c)** is the bb case. The colored spheres represent the vacancies

Model 2

The most stable surface in Model 2 was (111). This structure is a little bit more complicated for determining the possible O vacancies, since there are regions that do not show periodicity. That is why only two possibilities were considered for this model: **ov1**, with one vacancy and **ov2**, with two vacancies. Naturally, the O atoms that were removed were the top-most atoms. In Fig. 4.27 it is observed the results for both cases. Again the highlighted atoms are the O atoms that will be removed. After that, the surface energy was again calculated for this surfaces and the results are shown in Fig. 4.28. The same behaviour as in the case for Model 1 is observed, where the stoichiometric case shows more stability. In this scenario, it is possible to infer that for $\gamma - Al_2O_3$ it may be more

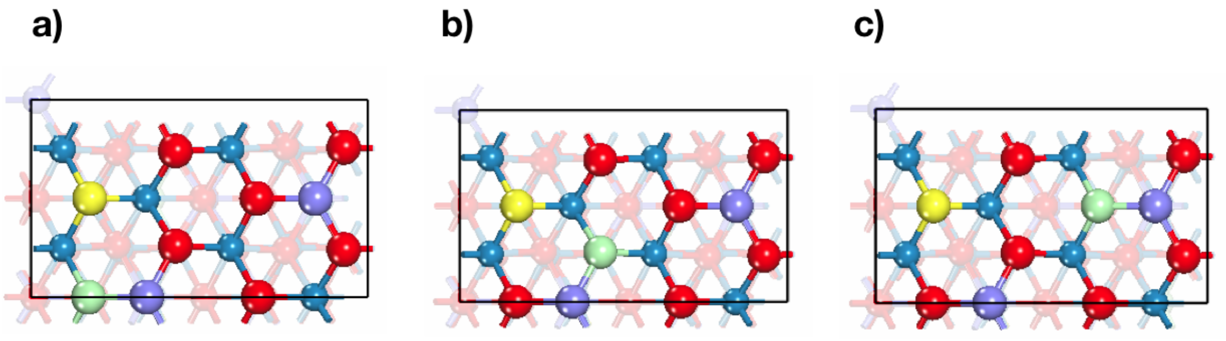

Figure 4.25: Non-stoichiometric surfaces with two vacancies of the different type, where **(a)** is the ab1 case, **(b)** is the ab2 case and **(c)** is the ab3 case. The colored spheres represent the vacancies

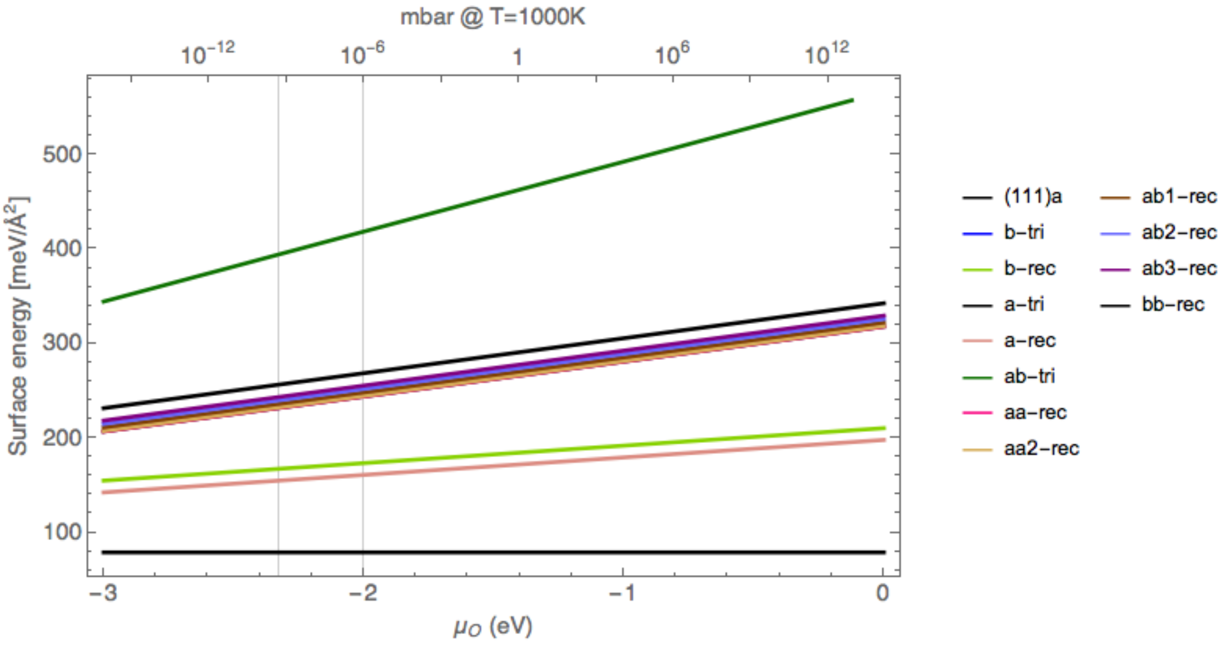

Figure 4.26: Surface energy of the non-stoichiometric surfaces of Model 1

favorable to have non-stoichiometric surfaces with an excess of O atoms instead of vacancies. Actually, for this work, a non-stoichiometric surface with an extra O atom was also studied, and the behaviour shows a great stability in the region of interest for μ_O values. However, the results cannot be shown here, since it was not possible to finish the energy calculations for this system.

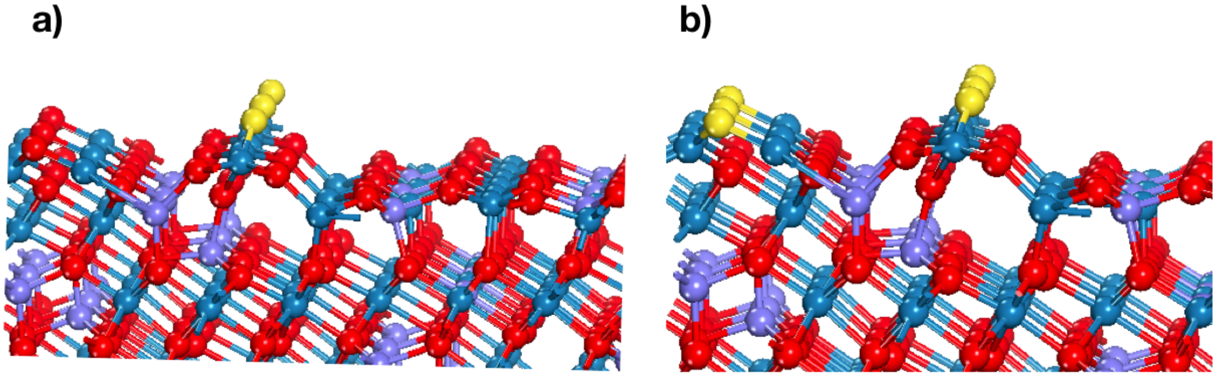

Figure 4.27: Non-stoichiometric surfaces of Model 2. **(a)** Type ov1 and **(b)** Type ov2. The colored spheres represent the vacancies

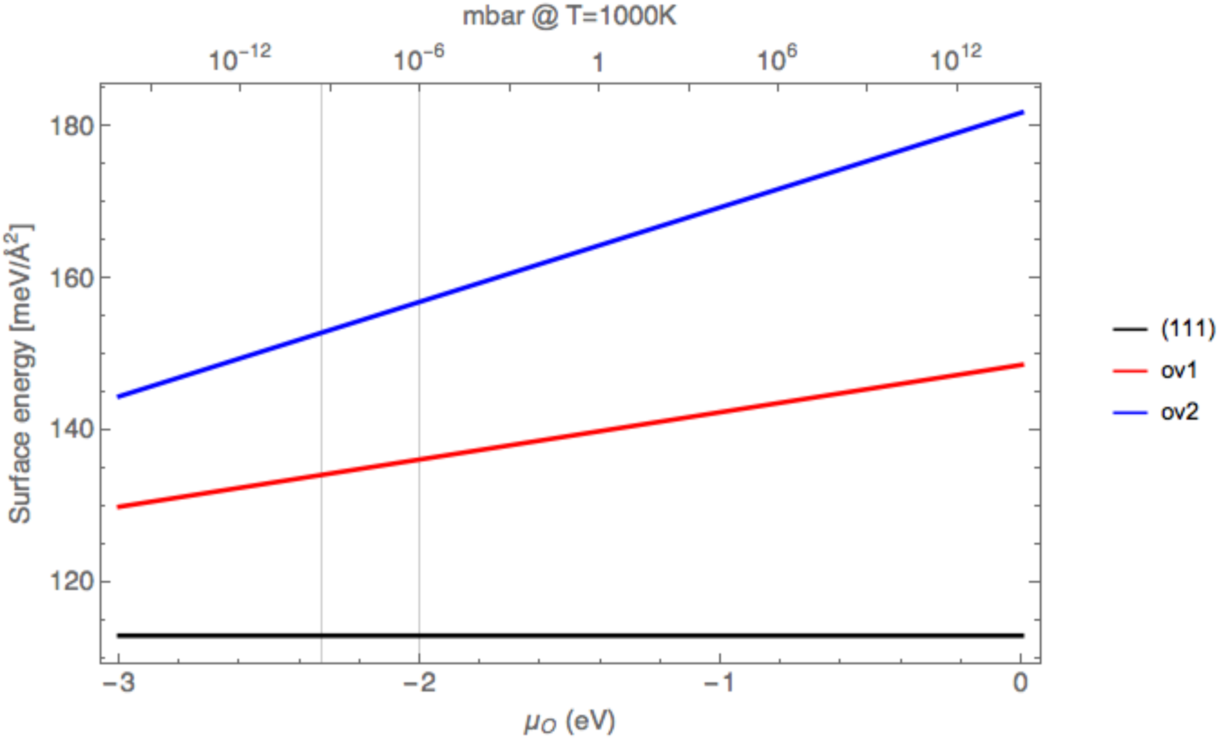

Figure 4.28: Surface energy of the non-stoichiometric surfaces of Model 2.

Chapter 5

Conclusions & Outlook

In this work, it was performed DFT calculations to study $\gamma - Al_2O_3$ surfaces. The main purpose was to test two atomic models (Model 1 and Model 2) from the literature using a SCAN functional that has a higher level of accuracy than the functionals used in the works where the models were introduced.

In the first stage, I performed the bulk structure optimization for both models and obtained the electronic structure results. In general, the crystallographic parameters like the lattice parameter values using SCAN were closer to the values obtained using GGA, but the Bulk modulus differ a lot. Also, the bandgaps values increase for both models with this functional and as was expected it yields a result closer to the experimental value.

After that, different stoichiometric surfaces were obtained from the bulk structures and the surface energy was computed to determine the most stable configurations. For Model 1, the most stable surfaces were $(111)a$ and $(001)a$, while for Model 2, the most stable surfaces were (111) and $(001)a$ in the cubic system. For Model 2, in surface (111), it was observed an interesting effect where an amorphous phase was formed in the films, and this effect was not shown for ultra-thin films. The structural relaxation calculations show that, in general, bare surfaces are most favorable than surfaces with lumps. Also, the Al_A atoms at the top yield more stable surfaces than Al_B atoms, but the most stable cases will always prefer a major concentration of O atoms at the top of the surface.

After this, UPS simulations were done for the most stable surfaces. It was observed that the biggest contributions come from the O atoms, specifically with the O_{2p} orbitals. Additionally, it is observed a small shoulder at the left of the major peak. This behaviour was the same for both models and it is similar to the experimental result where the differences are mainly in the peak positions and intensities. The UPS spectrum for the surface $(001)a - M1$ is the one that has the most similar shape compared to the experimental spectrum.

Additionally, non-stoichiometric surfaces were obtained from the surface $(111)a$ in Model 1, and surface (111) in Model 2, by generating O vacancies. For the Model 1, there were eleven different configurations to get a non-stoichiometric surface. It was distinguished between two types of vacancies (a and b), where the first one was connected to an Al_A atom and the latter, to an Al_B atom, as well as different geometrical configurations (trigonal and rectangular). For the Model 2, there were only two non-stoichiometric surfaces that were obtained by removing either one or two oxygen atoms at the top. The surface energy calculations, in this case, showed that the pressure range of interest, the stoichiometric surfaces are most favorable in both models.

There are still many questions that need to be addressed for this material. The results from this work can be used to validate these models with future experiments. The next stage in this research will include the extension of the work to other models and the exploration of other non-stoichiometric surfaces, by considering an excess of O atoms instead of vacancies.

Appendix A

PDOS of the computed surfaces

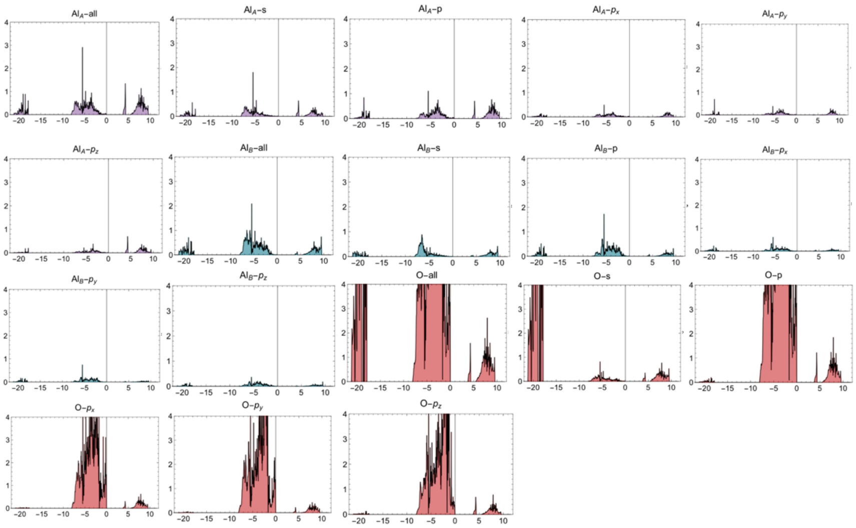

Figure A.1: Detailed computed PDOS for the surface (111)*a* studied in M1

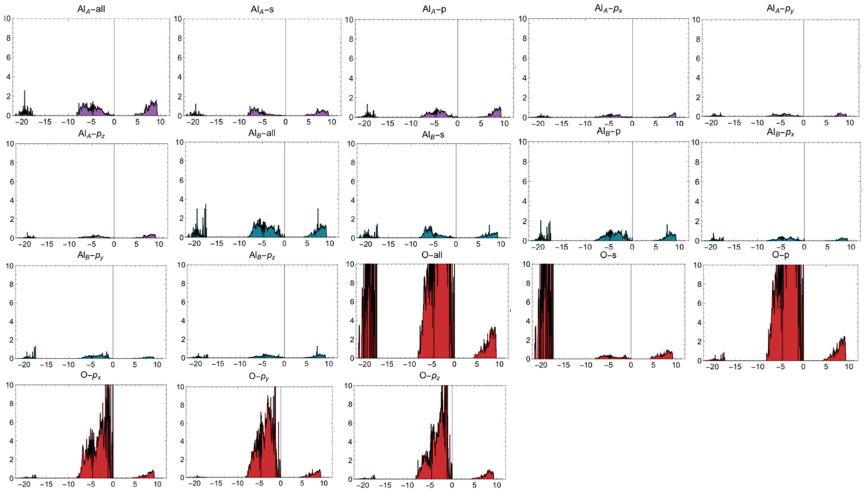

Figure A.2: Detailed computed PDOS for the surface (001)*a* studied in M1

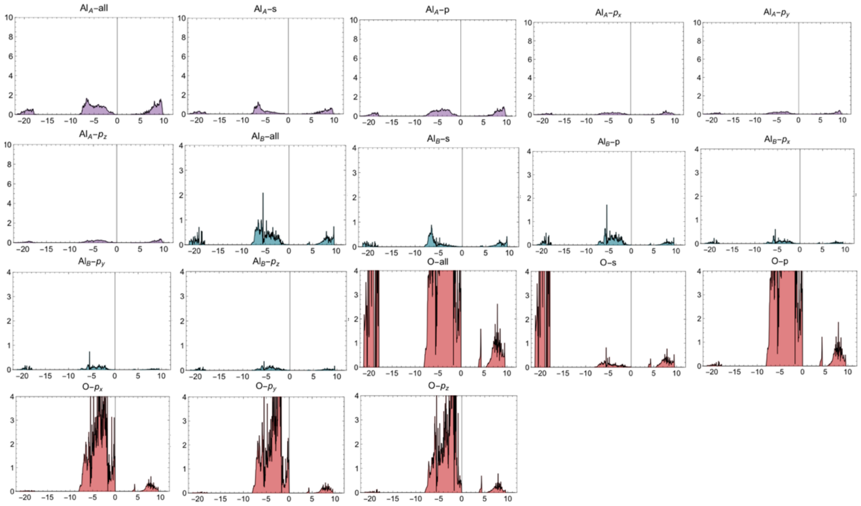

Figure A.3: Detailed computed PDOS for the surface (111) studied in M2

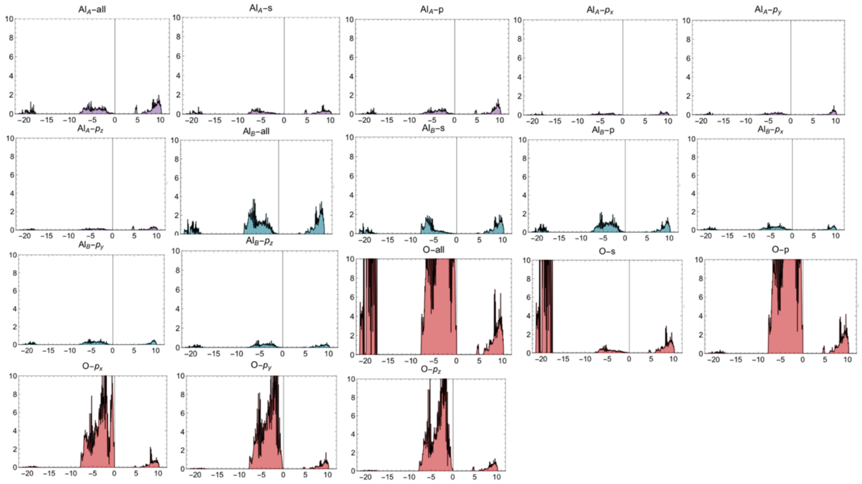

Figure A.4: Detailed computed PDOS for the surface (001)*a* studied in M2

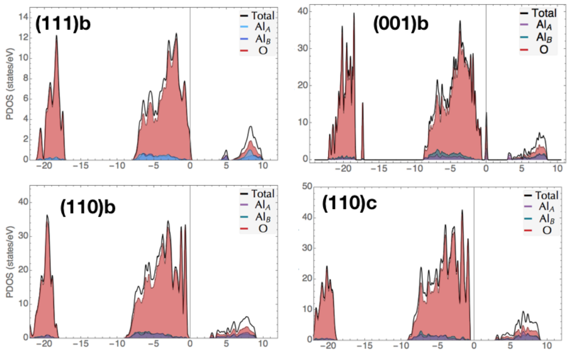

Figure A.5: PDOS of the rest of the surfaces generated for M1

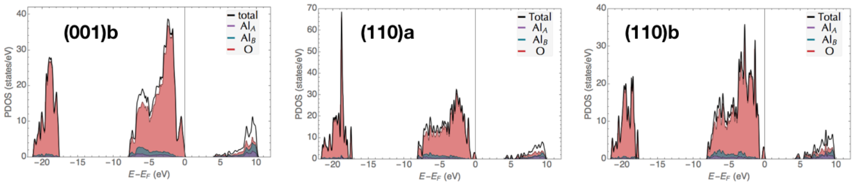

Figure A.6: PDOS of the rest of the surfaces generated for M2

Appendix B

IMFP and Photon Cross Section for the UPS

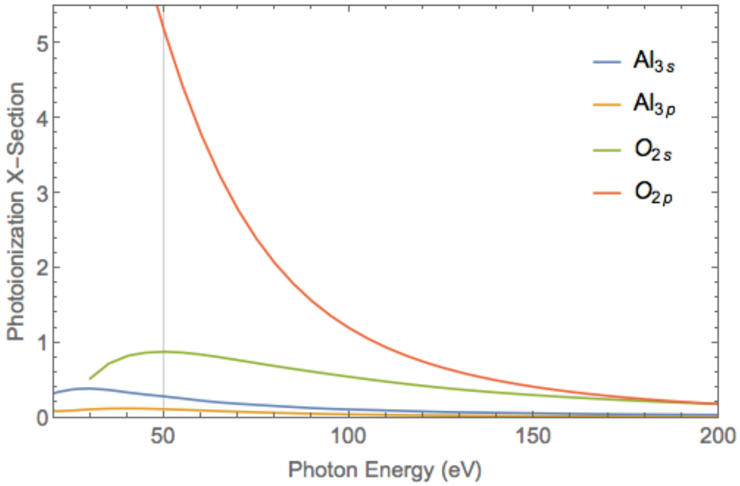

Figure B.1: Photoionization Cross Section used to simulate the UPS. Taken from ref.[7]

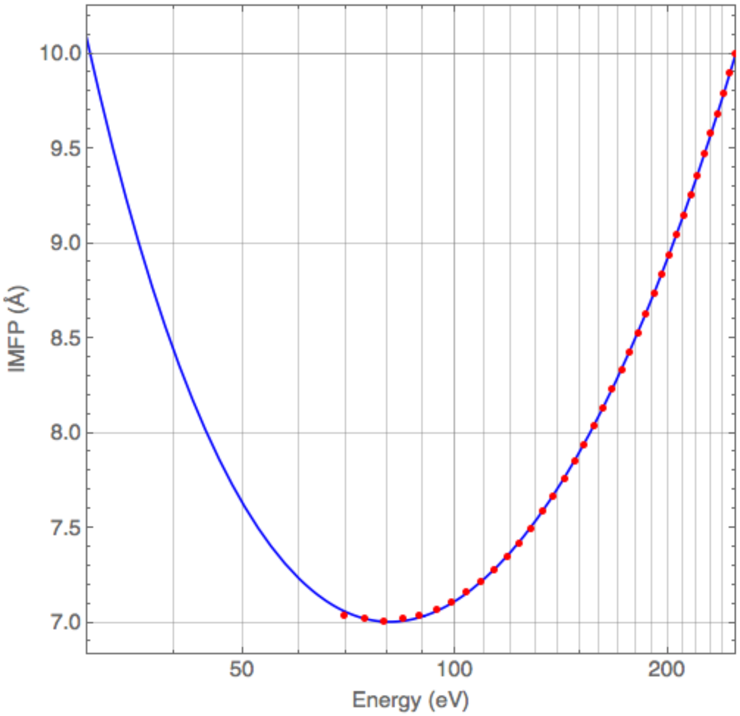

Figure B.2: IMFP used to simulate the UPS

Appendix C

Workfunctions computed for the most stable surfaces

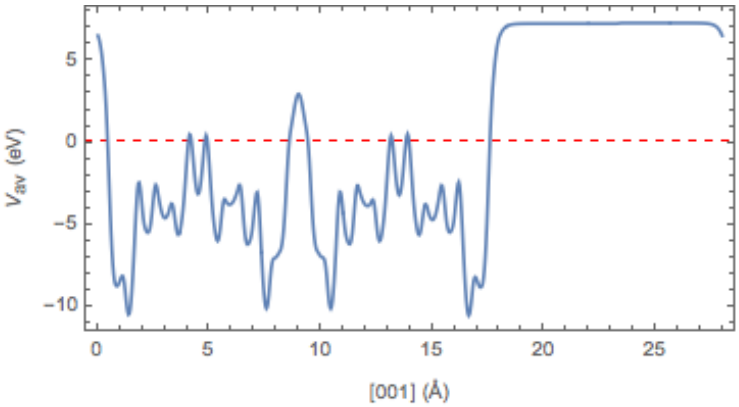

Figure C.1: Computed workfunction for the surface (111)*a* of M1

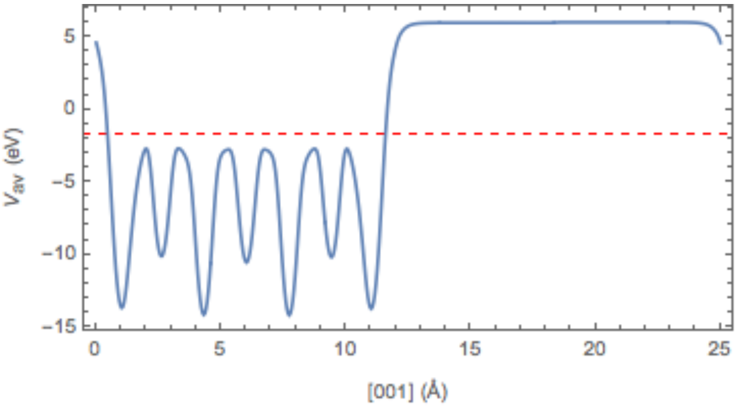

Figure C.2: Computed workfunction for the surface (001)*a* of M1

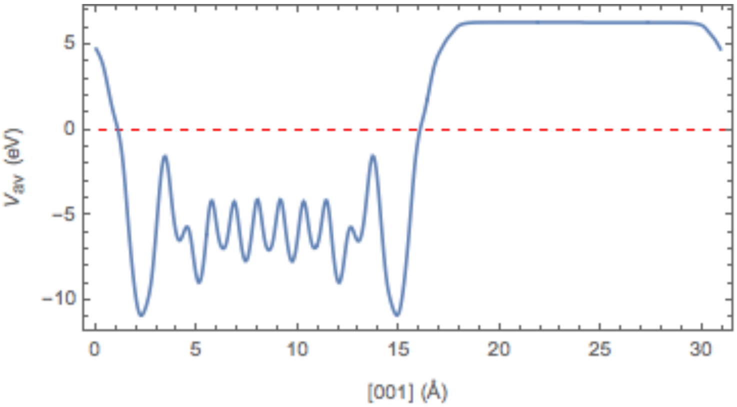

Figure C.3: Computed workfunction for the surface (111) of M2

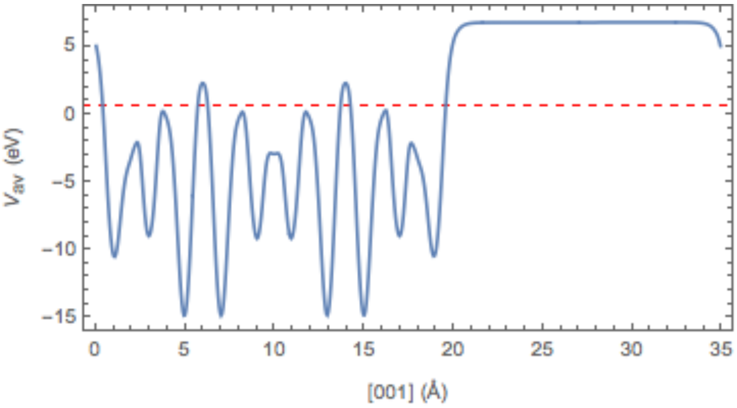

Figure C.4: Computed workfunction for the surface (001)*a* of M2

Bibliography

[1] Perdew, J. P.; Ruzsinszky, A.; Tao, J.; Staroverov, V. N.; Scuseria, G. E.; Csonka, G. I. Prescription for the design and selection of density functional approximations: More constraint satisfaction with fewer fits. *The Journal of chemical physics* **2005**, *123*, 062201.

[2] VASP, VASP Basics. 2019; `https://www.nersc.gov/assets/Uploads/VASP-lecture-Basics.pdf`, Online accessed: 13-May-2022.

[3] Kantorovich, L. *Quantum theory of the solid state: an introduction*; Springer Science & Business Media, 2004; Vol. 136.

[4] Seah, M. P.; Dench, W. Quantitative electron spectroscopy of surfaces: A standard data base for electron inelastic mean free paths in solids. *Surface and interface analysis* **1979**, *1*, 2–11.

[5] Powell, C.; Jablonski, A. NIST Electron Inelastic-Mean-Free-Path Database. 2010; `https://www.nist.gov/system/files/documents/srd/SRD71UsersGuideV1-2.pdf`, Online accessed: 1-Jun-2022.

[6] Jimenez-Gonzalez, A.; Schmeisser, D. Preparation and spectroscopic characterization of γ-Al2O3 thin films. *Surface science* **1991**, *250*, 59–70.

[7] Yeh, J.; Lindau, I. Atomic subshell photoionization cross sections and asymmetry parameters: 1 Z 103. *Atomic data and nuclear data tables* **1985**, *32*, 1–155.

[8] Hagen, J. *Industrial catalysis: a practical approach*; John Wiley & Sons, 2015.

[9] Catlow, C. R.; Davidson, M.; Hardacre, C.; Hutchings, G. J. Catalysis making the world a better place. 2016.

[10] Morterra, C.; Magnacca, G. A case study: surface chemistry and surface structure of catalytic aluminas, as studied by vibrational spectroscopy of adsorbed species. *Catalysis Today* **1996**, *27*, 497–532.

[11] McHale, J.; Auroux, A.; Perrotta, A.; Navrotsky, A. Surface energies and thermodynamic phase stability in nanocrystalline aluminas. *Science* **1997**, *277*, 788–791.

[12] Trueba, M.; Trasatti, S. P. γ-Alumina as a support for catalysts: a review of fundamental aspects. *European journal of inorganic chemistry* **2005**, *2005*, 3393–3403.

[13] Dry, M. E. Practical and theoretical aspects of the catalytic Fischer-Tropsch process. *Applied Catalysis A: General* **1996**, *138*, 319–344.

[14] Krebs, E.; Daudin, A.; Raybaud, P. A DFT study of CoMoS and NiMoS catalysts: From nano-crystallite morphology to selective hydrodesulfurization. *Oil & Gas Science and Technology-Revue de l'IFP* **2009**, *64*, 707–718.

[15] Digne, M.; Sautet, P.; Raybaud, P.; Euzen, P.; Toulhoat, H. Use of DFT to achieve a rational understanding of acid–basic properties of γ-alumina surfaces. *Journal of Catalysis* **2004**, *226*, 54–68.

[16] Stuart, N. M.; Sohlberg, K. The Microstructure of γ-Alumina. *Energies* **2021**, *14*, 6472.

[17] Prins, R. On the structure of γ-Al2O3. *Journal of Catalysis* **2020**, *392*, 336–346.

[18] Zamorategui M, A.; Ramírez R, N.; Martínez R, J. M.; Serafín M, A. H. Synthesis and characterization of gamma alumina and compared with an activated charcoal on the fluoride removal from potable well water. *Acta universitaria* **2016**, *26*, 30–35.

[19] Ayoola, H. O.; House, S. D.; Bonifacio, C. S.; Kisslinger, K.; Saidi, W. A.; Yang, J. C. Evaluating the accuracy of common γ-Al2O3 structure models by selected area electron diffraction from high-quality crystalline γ-Al2O3. *Acta Materialia* **2020**, *182*, 257–266.

[20] Verwey, E. The crystal structure of γ-Fe2O3 and γ-Al2O3. *Zeitschrift für Kristallographie-Crystalline Materials* **1935**, *91*, 65–69.

[21] Raybaud, P.; Chizallet, C.; Mager-Maury, C.; Digne, M.; Toulhoat, H.; Sautet, P. From γ-alumina to supported platinum nanoclusters in reforming conditions: 10 years of DFT modeling and beyond. *Journal of catalysis* **2013**, *308*, 328–340.

[22] Pigeon, T.; Chizallet, C.; Raybaud, P. Revisiting γ-alumina surface models through the topotactic transformation of boehmite surfaces. *Journal of Catalysis* **2022**, *405*, 140–151.

[23] Smrčok, L.; Langer, V.; Křest'an, J. γ-Alumina: a single-crystal X-ray diffraction study. *Acta Crystallographica Section C: Crystal Structure Communications* **2006**, *62*, i83–i84.

[24] Pinto, H. P.; Nieminen, R. M.; Elliott, S. D. Ab initio study of γ- Al 2 O 3 surfaces. *Physical review B* **2004**, *70*, 125402.

[25] Paglia, G.; Buckley, C.; Rohl, A.; Hunter, B.; Hart, R.; Hanna, J.; Byrne, L. Tetragonal structure model for boehmite-derived γ-alumina. *Physical Review B* **2003**, *68*, 144110.

[26] Zhou, R.-S.; Snyder, R. L. Structures and transformation mechanisms of the η, γ and θ transition aluminas. *Acta Crystallographica Section B: Structural Science* **1991**, *47*, 617–630.

[27] Griffiths, D. J.; Schroeter, D. F. *Introduction to quantum mechanics*; Cambridge university press, 2018.

[28] Giustino, F. *Materials modelling using density functional theory: properties and predictions*; Oxford University Press, 2014.

[29] Patterson, J. D.; Bailey, B. C. *Solid-State Physics*; Springer, 2018; pp 649–704.

[30] Kurth, S.; Marques, M.; Gross, E. In *Encyclopedia of Condensed Matter Physics*; Bassani, F., Liedl, G. L., Wyder, P., Eds.; Elsevier: Oxford, 2005; pp 395–402.

[31] Jungwirth, P. Density Functional Theory. A Practical Introduction. By David Sholl and Janice A. Steckel. 2010.

[32] Lee, J. G. *Computational materials science: an introduction*; CRC press, 2016.

[33] Kittel, C.; McEuen, P. *Kittel's Introduction to Solid State Physics*; John Wiley & Sons, 2018.

[34] Mardirossian, N.; Head-Gordon, M. Thirty years of density functional theory in computational chemistry: an overview and extensive assessment of 200 density functionals. *Molecular Physics* **2017**, *115*, 2315–2372.

[35] Ceperley, D. M.; Alder, B. J. Ground state of the electron gas by a stochastic method. *Physical review letters* **1980**, *45*, 566.

[36] Sun, J.; Furness, J. W.; Zhang, Y. *Mathematical Physics in Theoretical Chemistry*; Elsevier, 2019; pp 119–159.

[37] Gross, A. Theoretical surface science. *A Microscopic Perspective. Originally published in the series: Advanced Texts in Physics,* **2003**, *132*.

[38] Sun, J.; Ruzsinszky, A.; Perdew, J. P. Strongly constrained and appropriately normed semilocal density functional. *Physical review letters* **2015**, *115*, 036402.

[39] Sun, J.; Remsing, R. C.; Zhang, Y.; Sun, Z.; Ruzsinszky, A.; Peng, H.; Yang, Z.; Paul, A.; Waghmare, U.; Wu, X.; *et al.*, Accurate first-principles structures and energies of diversely bonded systems from an efficient density functional. *Nature chemistry* **2016**, *8*, 831–836.

[40] Sholl, D. S.; Steckel, J. A. *Density functional theory: a practical introduction*; John Wiley & Sons, 2011.

[41] Blöchl, P. E. Projector augmented-wave method. *Physical review B* **1994**, *50*, 17953.

[42] Ozawa, K. *Compendium of Surface and Interface Analysis*; Springer, 2018; pp 783–790.

[43] Kuzmany, H. *Solid-state spectroscopy: an introduction*; Springer, 2009.

[44] Schaible, M. J.; Pinto, H. P.; McKee, A. D.; Leszczynski, J.; Orlando, T. M. Characterization and simulation of natural pyrite surfaces: a combined experimental and theoretical study. *The Journal of Physical Chemistry C* **2019**, *123*, 26397–26405.

[45] Ellis, A. M.; Fehér, M.; Wright, T. G. *Electronic and photoelectron spectroscopy: fundamentals and case studies*; Cambridge University Press, 2005.

[46] Łodziana, Z.; Topsøe, N.-Y.; Nørskov, J. K. A negative surface energy for alumina. *Nature materials* **2004**, *3*, 289–293.

[47] Tran, R.; Xu, Z.; Radhakrishnan, B.; Winston, D.; Sun, W.; Persson, K. A.; Ong, S. P. Surface energies of elemental crystals. *Scientific data* **2016**, *3*, 1–13.

[48] Boettger, J. Nonconvergence of surface energies obtained from thin-film calculations. *Physical Review B* **1994**, *49*, 16798.

[49] Reuter, K.; Scheffler, M. Composition, structure, and stability of RuO 2 (110) as a function of oxygen pressure. *Physical Review B* **2001**, *65*, 035406.

[50] Wang, X.-G.; Chaka, A.; Scheffler, M. Effect of the Environment on α- Al 2 O 3 (0001) Surface Structures. *Physical Review Letters* **2000**, *84*, 3650.

[51] Wang, X.-G.; Weiss, W.; Shaikhutdinov, S. K.; Ritter, M.; Petersen, M.; Wagner, F.; Schlögl, R.; Scheffler, M. The hematite (α-Fe 2 O 3)(0001) surface: evidence for domains of distinct chemistry. *Physical Review Letters* **1998**, *81*, 1038.

[52] Chase Jr, M.; Curnutt, J.; Downey Jr, J.; McDonald, R.; Syverud, A.; Valenzuela, E. JANAF thermochemical tables, 1982 supplement. *Journal of Physical and Chemical Reference Data* **1982**, *11*, 695–940.

[53] Kresse, G. VASP, Vienna ab initio simulation package, 2004. *URL: https://www. vasp. at*

[54] Lejaeghere, K.; Bihlmayer, G.; Björkman, T.; Blaha, P.; Blügel, S.; Blum, V.; Caliste, D.; Castelli, I. E.; Clark, S. J.; Dal Corso, A.; *et al.*, Reproducibility in density functional theory calculations of solids. *Science* **2016**, *351*, aad3000.

[55] Monkhorst, H. J.; Pack, J. D. Special points for Brillouin-zone integrations. *Physical review B* **1976**, *13*, 5188.

[56] Wisesa, P.; McGill, K. A.; Mueller, T. Efficient generation of generalized Monkhorst-Pack grids through the use of informatics. *Physical Review B* **2016**, *93*, 155109.

[57] Tyuterev, V.; Vast, N. Murnaghan's equation of state for the electronic ground state energy. *Computational materials science* **2006**, *38*, 350–353.

[58] Tanuma, S.; Powell, C. J.; Penn, D. R. Calculations of electron inelastic mean free paths. V. Data for 14 organic compounds over the 50–2000 eV range. *Surface and interface analysis* **1994**, *21*, 165–176.

[59] Liu, R.; Elleuch, O.; Wan, Z.; Zuo, P.; Janicki, T. D.; Alfieri, A. D.; Babcock, S. E.; Savage, D. E.; Schmidt, J.; Evans, P. G.; *et al.*, Phase Selection and Structure of Low-Defect-Density γ-Al2O3 Created by Epitaxial Crystallization of Amorphous Al2O3. *ACS Applied Materials & Interfaces* **2020**, *12*, 57598–57608.

[60] Ealet, B.; Elyakhloufi, M.; Gillet, E.; Ricci, M. Electronic and crystallographic structure of γ-alumina thin films. *Thin solid films* **1994**, *250*, 92–100.

[61] Castro, R. H.; Ushakov, S. V.; Gengembre, L.; Gouvêa, D.; Navrotsky, A. Surface energy and thermodynamic stability of γ-alumina: Effect of dopants and water. *Chemistry of materials* **2006**, *18*, 1867–1872.

[62] McHale, J.; Navrotsky, A.; Perrotta, A. Effects of increased surface area and chemisorbed H2O on the relative stability of nanocrystalline γ-Al2O3 and α-Al2O3. *The Journal of Physical Chemistry B* **1997**, *101*, 603–613.

[63] Castro, R. H.; Quach, D. V. Analysis of anhydrous and hydrated surface energies of gamma-Al2O3 by water adsorption microcalorimetry. *The Journal of Physical Chemistry C* **2012**, *116*, 24726–24733.